Chapter 1.0 Introduction

Since the implementation of gas turbine engines for the purpose of aircraft propulsion, continuous progress has been made in their performance, reliability, and efficiency. However, there remains a continuing need for continued improvement with regard to noise, cost, efficiency, power, safety, and weight. Unfortunately, an improvement in any one of these areas will often lead to detrimental effects in another area. Therefore, different types of aircraft have specific engine design criteria which are optimized for the particular application. In response to the demand for improved aircraft gas turbine engine performance, a great deal of research has focused on enhancing the design of axial-flow compressors.

The two available means of evaluating new compressor designs are experimental and computational. The advantages of experimental testing are more accurate and reliable results. Therefore, physical experimental testing is required prior to implementation of a new design. The advantages of computational simulation are speed, reduced cost, more data, and rapid design modifications. Due to time and cost considerations involved in experimental testing of new compressors, computational simulations have been used more extensively in recent years. Through the use of advanced and accurate computer simulations, much of the preliminary experimental testing may be eliminated.

Three-dimensional computational fluid dynamic (CFD) codes are highly sophisticated and require a great deal of computation time. In addition, 3-D CFD codes require accurate turbulence models which are currently unavailable. As a result of these limitations, less complex psuedo-3-D Streamline Curvature Codes (SLCC), which provide a spanwise prediction of thermodynamic and other flow variables, are still widely used (Cetin, 1987).

The SLCC Compressor Performance Analysis Code (CPAC) was originally developed by Hearsey (1970) and later modified by Hale (1996). CPAC has the ability to use correlations to obtain stage-by-stage characteristics, which for an axial-flow flow compressor are the pressure ratio and the efficiency with respect to corrected mass flow rates at various speeds. These correlations specify blade total pressure loss and flow deviation from the blade exit geometry, which encompass the physical phenomena that the blade geometry imposes on the flow field. Loss and deviation correlations implement theory from geometric effects, boundary layers, and shocks in an effort to match the empirical results.

Current correlations in CPAC are inaccurate for high-speed transonic axial-flow flow compressors. The correlations used in industry are likely to be more accurate but are usually proprietary. However, additional correlations are available in the open literature. The primary goal of the present correlation studies was to obtain accurate loss and deviation models for use in an SLCC. Due to the complexity of this task, the effort was divided into parts. The logical method for this breakdown was to use a 1-D compressible flow code to investigate loss correlations along a solitary streamline as opposed to attempting an entire spanwise flow prediction. The streamline chosen for this initial investigation was that located at the mid-span of the blade, often referred to as the meanline. The purpose of the meanline analysis was to provide a simple method of gathering insights on the behavior and quality of the correlations. In addition, losses due to hub and casing boundary layers are negligible at the meanline, as are many secondary flow effects. It is also beneficial that because radial effects can be neglected, the radius of the meanline streamline remains relatively constant as opposed to the radii of hub and tip streamlines.

It is hypothesized that the correlations which best represent the data at the meanline will also perform adequately for the majority of the remainder of the flowfield. This is due to the fact that loss and deviation at the meanline are functions of the behavior of the flowfield along the entire span of the blade.

The objective of this research was to identify, investigate the theoretical validity, and evaluate the performance of the available correlations for use in SLCCs using a meanline analysis.

Chapter 2.0 contains background information, such as fundamentals of cascade aerodynamics, definitions of loss and deviation, and their correlations. Chapter 3.0 describes the approach and methods of gathering correlation information. Chapter 4.0 provides results and discussion and an evaluation of the models against experimental data. Chapter 5.0 contains general conclusions and recommendations for improvement and further evaluation of loss and deviation correlations.

Chapter 2.0 Background

Two-dimensional cascades and 2-D cascade theory are commonly used to model flow in transonic compressors because they better isolate the effects of the individual loss mechanisms such as shocks and boundary layers. The flow field inside a transonic compressor is extremely complex, being viscous, compressible, unsteady, 3-D, and containing both laminar and turbulent regions. This chapter will introduce cascade aerodynamics and describe loss and deviation for 2-D linear and 3-D annular cascades. A summary of the currently available loss and deviation models is included in this chapter as well.

2.1 Fundamentals of Cascade Aerodynamics

The objective of this section is to define terminology, definitions, notation, and sign convention used in 2-D linear cascade analysis. Figure 2.1 illustrates the absolute and relative flow velocities in an axial-flow flow cascade.

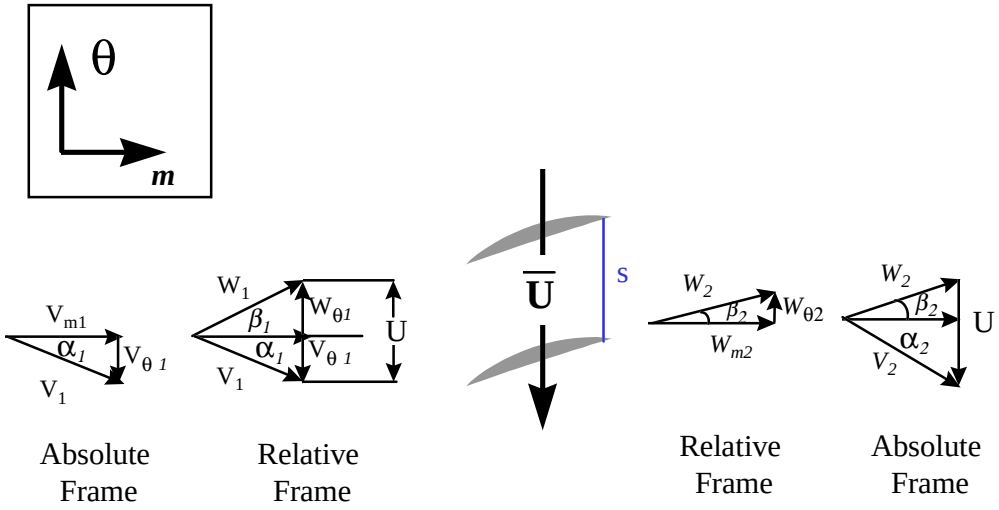

Figure 2.1 Axial-flow Compressor Cascade Geometry and Velocity Triangles

As the cascade blades are moving with velocity U in the -θ direction, it is convenient to view the fluid velocity from the perspective of a cascade blade in order to simplify blade row performance evaluation. This is known as switching from the absolute to the relative frame of reference. The absolute velocities and flow angles are expressed as V_i and α_i, respectively, and the relative velocities and flow angles are expressed as W_i and β_i, respectively. In order to relate absolute to relative reference frames or vice versa, one need only apply the vector sum as shown in Equation 2.1.

$$\overline{\mathbf{W}} = \overline{\mathbf{V}} - \overline{\mathbf{U}} \qquad \textbf{(2.1)}$$

Loss and deviation correlations are presented as functions of blade geometry. Therefore, it is critical to understand blade terminology in order to correctly apply the correlations. Figure 2.2 is a schematic of a blade with several definitions noted.

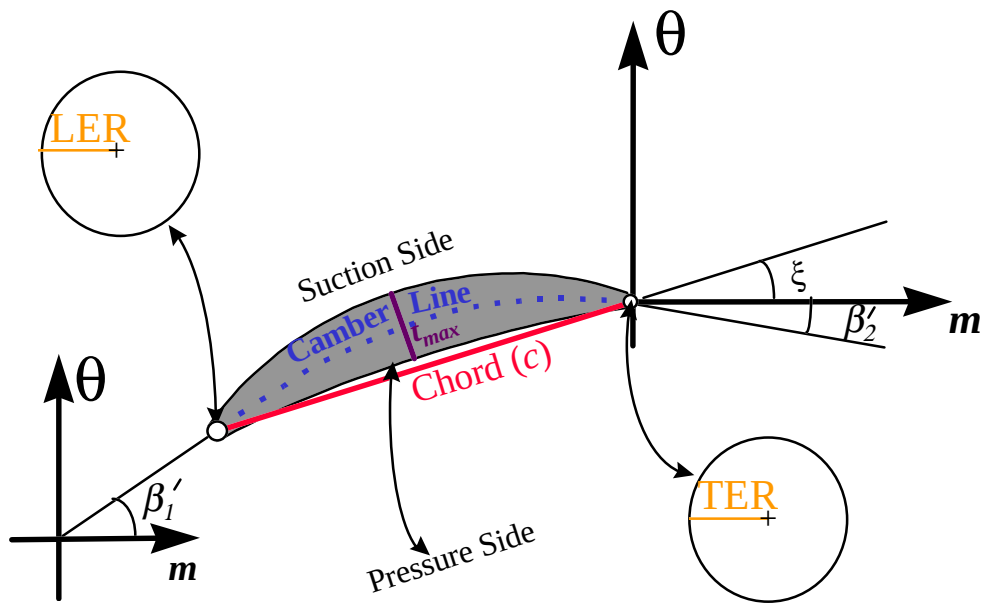

.

Figure 2. 2 Axial-flow Compressor Blade Geometry

In Figure 2.2, the chord (c) is the distance from the leading edge to the trailing edge of the airfoil. The leading edge radius (LER) and trailing edge radius (TER) are used to measure the blade thickness at the inlet and exit of the blade. The camber line is that line which represents the mid-thickness of the blade between its pressure and suction sides at every point along the airfoil. The length of the camber line is often referred to as the camber length. The blade angles (β'_1) and (β'_2), also called the metal angles, are those between the meridional axis (m) and the line tangent to the camber line at the blade

leading and trailing edges, respectively. Deviation (δ) is defined as the difference between the exit relative flow angle (β'_2) and the blade exit metal angle (β'_2) (see Equation 2.3). The angle formed between the chord line and the meridional axis is referred to as the stagger angle (ξ). The maximum thickness between the pressure and suction sides of the airfoil is (t_{max}). Although not shown in Figure 2.2, *a* is the distance along the chord from the leading edge of the blade to the point of maximum camber, which occurs where there is maximum displacement between the camber line and the chord line. The spacing (*s*) is the distance between blades in the θ direction. Equations 2.2 through 2.6 represent some blade geometry definitions as expressed in equation form:

$$i = \beta_1 - \beta'_1 \qquad \textbf{(2.2)}$$

$$\delta = \beta_2 - \beta'_2 \qquad \textbf{(2.3)}$$

$$\alpha^* = \beta_1 - \xi \qquad \textbf{(2. 4)}$$

$$\theta' = \beta'_1 - \beta'_2 \qquad \textbf{(2. 5)}$$

$$\sigma = \frac{s}{c} \qquad \textbf{(2. 6)}$$

These geometry definitions include the incidence angle (i), deviation angle (δ), angle of attack (α^*), camber angle (θ'), and cascade solidity (σ).

2.2 Loss and Deviation Correlations

Loss and deviation correlations are used to describe the physics of entropy generation and fluid turning in axial-flow compressors. For a 2-D compressor cascade, loss ($\bar{\omega}$) is defined as the nondimensionalized ratio of the difference between inlet total pressure and exit total pressure to the inlet dynamic pressure (see Figure 2.3 and Equation 2.7).

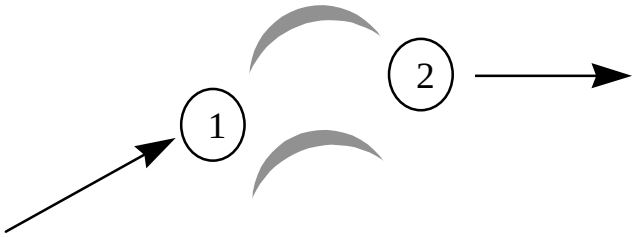

Figure 2.3. Diagram of Inlet and Exit of a 2-D Cascade

$$\bar{\omega} = (P_{t1} - P_{t2}) / (P_{t1} - P_1) \qquad \textbf{(2.7)}$$

In Equation 2.7, P_{t1} and P_{t2} are the inlet and exit total pressures, respectively, and P_1 is the static pressure at the cascade inlet plane.

Loss represents the entropy generated due to shocks, boundary layers, secondary losses, and mixing, as well as that generated by interactions between them. Loss models which can quantify accurately these interactions are beyond the state of the art (Bloch, 1996). It is common practice to assume linearity and to estimate the total loss by superposition of the individual loss terms (see Equation 2.8) (Moses, 1994, Cetin, 1987).

$$\bar{\omega} \cong \bar{\omega}_{SH} + \bar{\omega}_{PR} + \bar{\omega}_{S} \qquad \textbf{(2.8)}$$

In Equation 2.8, $\bar{\omega}_{SH}$ is the loss due to shocks, $\bar{\omega}_{PR}$ is the profile loss due to boundary layers, and $\bar{\omega}_{S}$ is the loss caused by secondary flow effects. The present author discovered that there exists a more thermodynamically sound method of quantifying the

total loss by superposition of entropy generation terms as opposed to the traditional superposition of loss terms (see Appendix D). However, at the low levels of losses experienced in a well-designed transonic compressor, the difference between the total loss calculated by superposition of pressure losses as opposed to that calculated by entropy generation is found to be negligible. In addition, because loss mechanisms do not behave completely linearly, either method provides a satisfactory approximation of the total loss.

If the loss and deviation are known in addition to the blade geometry and inlet conditions, the streamline curvature simulation can obtain exit flow thermodynamic and fluid mechanic properties. Unfortunately, there is no strictly theoretical means of obtaining loss or deviation. However, simple analyses may be employed to provide useful insights, and combined with empirical information can provide a satisfactory basis for cascade design (Hill & Peterson, 1967).

As stated previously, 2-D cascades and 2-D cascade theory are commonly used to model flow in transonic compressors. Note that 2-D linear cascade data and theory must be modified in order to prepare them for use in modeling an actual 3-D compressor flowfield. Some adjustments in converting from a 2-D to a 3-D flowfield include:

1) New definition of loss to account for change in radius
2) Conversion from 2-D to 3-D loss
3) Converting 2-D Axial Velocity Density Ratio to analogous 3-D Meridional Velocity Density Ratio
4) Introduction of new losses such as those due to mid-span dampers, casing and hub boundary layers, vortices between the casing and the rotor tip, and additional secondary losses which are not present in strictly 2-D flowfields.

The definition of the above terms and their application to loss modeling will be explained in subsequent sections.

Modern transonic compressors have variable area annuli which force the engine modeler to account for changes in fluid flow properties as a function of radius when converting from a 2-D to a 3-D flowfield. As a result, a new definition of loss is required as well. The difference between definitions of loss for 2-D and 3-D flowfields is that the 3-D loss $\overline{\omega}_{3D}$ uses the ideal exit total pressure $P_{tr2ideal}$ as opposed to the inlet total pressure P_{t1} used in Equation 2.7 for the 2-D case (see Equation 2.9).

$$\overline{\omega}_{3D} = \frac{P_{tr2\ ideal} - P_{tr2}}{P_{tr1} - P_1} \qquad \textbf{(2.9)}$$

The change in reference total pressure from $P_{tr2ideal}$ to P_{tr1} is a result of assuming isentropic flow of a perfect gas along a streamline with no loss, heat transfer, or irreversible work. Constant rothalpy is a key requirement that allows the assumption of isentropic flow between state points (1) and (2) as shown in Figure 2.4 (Lieblein Chapter 7, 1965). Equation 2.10 shows the thermodynamic relationship between $P_{t2ideal}$ and P_{t1} which accounts for the centripetal effect of a radius change such as that shown in Figure 2.4.

$$\frac{P_{t2\ ideal}}{P_{t1}} = \left\{1 + \frac{\gamma-1}{2} * \frac{(\Omega\, r_2)^2}{\gamma\, R\, T_{t1}} \left[1 - (r_1/r_2)^2\right]\right\}^{\gamma/(\gamma-1)} \qquad \textbf{(2.10)}$$

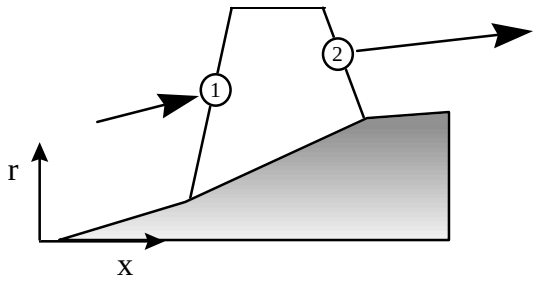

Figure 2.4 Meridional View of Radius Change due to Variable-Area Annulus

Many modern compressor simulations assume 3-D loss terms to be equivalent to those obtained in the 2-D case and neglect centrifugal effects introduced when converting from 2-D linear to 3-D annular cascades. The derivation in Appendix E illustrates a method of converting the 2-D loss to a 3-D loss. This derivation results in a relationship between $\overline{\omega}_{2D}$ and $\overline{\omega}_{3D}$ such as that shown in Equation 2.11.

$$\overline{\omega}_{3D} \cong (P_{tr2ideal} / P_{tr1}) * \overline{\omega}_{2D} \qquad \textbf{(2.11)}$$

An additional adjustment in converting from a 2-D to a 3-D flowfield is manipulating the 2-D Axial Velocity Density Ratio (AVDR) into an analogous 3-D Meridional Velocity Density Ratio (MVDR). The AVDR, as shown in Figure 2.12, is widely used to measure the degree to which the flow streamtubes in a 2-D cascade are contracted due to increasing density and decreasing area (Shreiber, 1984).

$$\textbf{AVDR} = (\rho_2 V_{x2}) / (\rho_1 V_{x1}) = A_{x1}/A_{x2} \qquad \textbf{(2.12)}$$

In Equation 2.12, ρ is the density, V_x the absolute axial velocity, A_x is the cross sectional area perpendicular to the axial, and the subscripts (1) and (2) imply the inlet and exit of the blade rows, respectively. The value of the AVDR is normally quoted when listing results from 2-D linear cascades. When applying these results to the prediction of the performance of 3-D annular cascades, the AVDR must be altered so as to apply to the corresponding 3-D annular flow. In this investigation, a new parameter, the MVDR, was developed to account for boundary layer effects in 3-D annular cascades. The development relating the definition of the MVDR to the AVDR is found in Appendix C.

Losses such as those due to mid-span dampers, casing and hub boundary layers, vortices between the casing and the rotor tip, and additional secondary losses not present in 2-D linear cascades must be obtained using experimental data from 3-D annular cascades. One approach to obtain these losses is to subtract the analytically calculated profile and shock losses in 2-D linear cascades from the experimentally obtained total loss in 3-D annular cascades.

Even with the aforementioned modifications, there remains no perfect method of quantifying some 3-D loss mechanisms due to the fact that they cannot be related to a presumably equivalent 2-D linear cascade (Serovy, 1989). However, the current methods are considered sufficiently accurate when augmented by 3-D effects obtained using 3-D CFD codes (Bloch, 1996).

Figure 2.5 illustrates a typical compressor performance map of total pressure ratio versus corrected mass rate of flow and indicates the stability line, stability margin, constant rotor corrected speed lines, and design point.

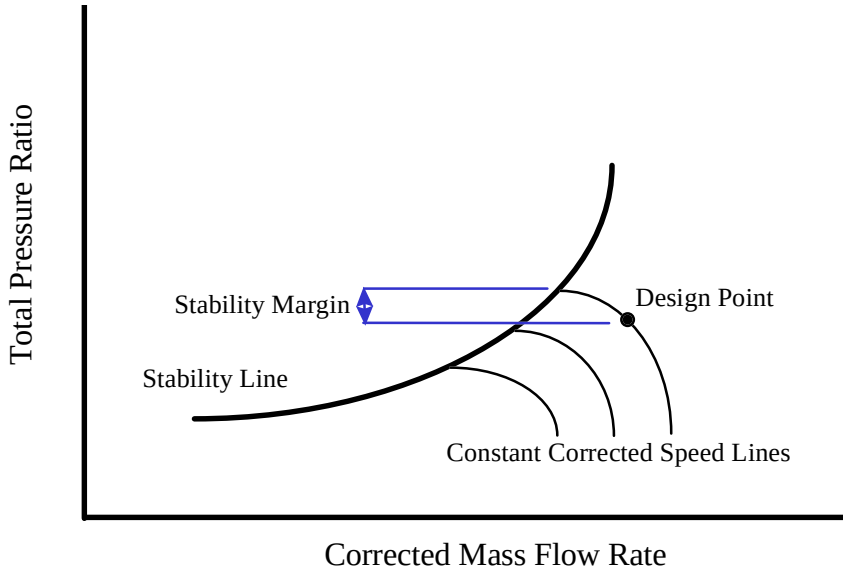

Figure 2.5 Performance Map of Axial-flow Compressor

The design point of a compressor lies on the 100% design speed line and indicates maximum performance with the given stability margin. Off-design conditions are defined as being at any point other than the design point on the compressor map, regardless of operational speed. Although the compressor often spends much of its lifetime at off-design conditions, the design point is still regarded as the most critical point on the map.

The stability line of a compressor is created by maintaining a constant compressor rotational speed and closing the exit throttle. This moves the operational condition of the compressor toward a decreased corrected mass flow rate and increased total pressure ratio along that same speed line. The performance of the machine improves until it reaches a point of unstable operation and an undesirable breakdown in machine performance. The stability line is the locus of these stability points for each of the constant corrected rotor speeds.

Since the design point is defined as being close to the maximum efficiency, minimum-loss for the 100% speed typically occurs at or near the design point. Many investigators have also applied design loss theory to minimum-loss points that occur at off-design compressor speeds, with moderate success. In order to obtain an accurate design point stage characteristic, one must not only calculate an accurate design loss, but accurate design incidence and deviation angles as well.

Currently, most off-design correlations use implicit or explicit methods in which one of the most important variables is the difference between the design and the off-design incidences. When a range of incidences for the 100% speed line is plotted, the off-design losses usually "bucket" around the design point, where the design point is regarded as the point of minimum-loss (see Figure 2.6). Off-minimum-loss deviation angle is predicted in a similar fashion.

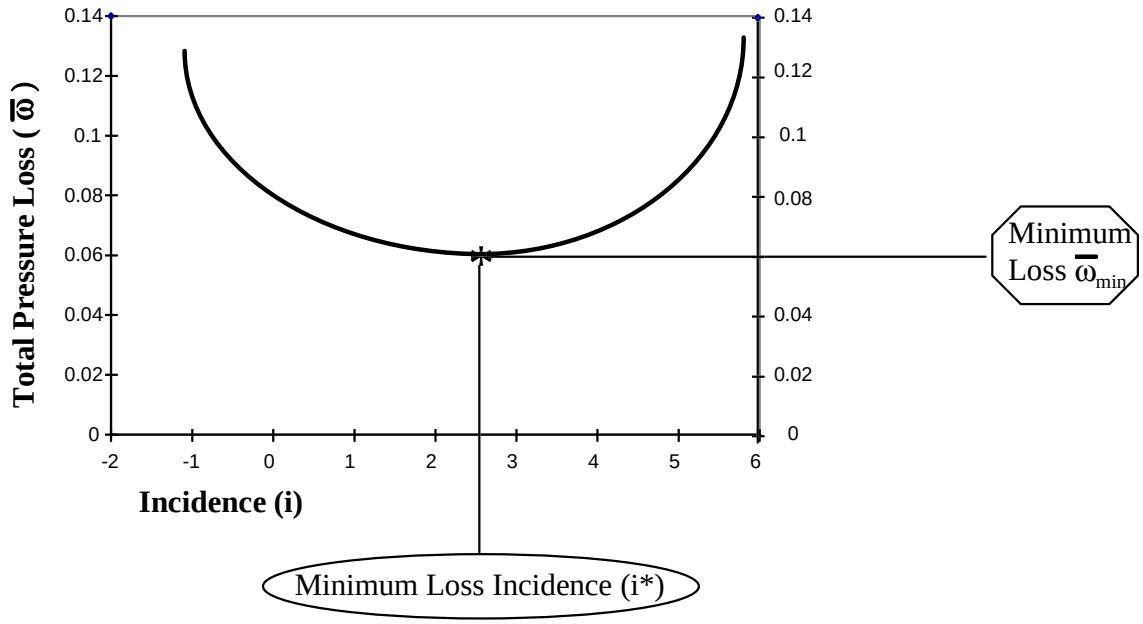

Figure 2.6 Plot of Loss versus Incidence for 100% Speed Line

2.3 Review of Correlations in the Open Literature

Minimum-loss incidence is defined as the incidence angle (i*) which has the lowest loss for a particular inlet relative Mach number. Lieblein (SP-36 Ch. 6, 1965) correlates minimum-loss incidence for a 2-D cascade as shown in Equation 2.13.

$$i^* = (K_{sh})(K_t)(i_{0_{10}}) + n\theta \qquad \textbf{(2.13)}$$

In Equation 2.13, (i^*) is the minimum-loss incidence, $(i_{0_{10}})$ is the uncambered minimum-loss incidence for a 10% t_{max}/c for a NACA $65A_{10}$ airfoil, (K_{sh}) is the correction factor due to thickness distribution, (K_t) is the correction factor due to the actual t_{max}/c, (n) is the slope of the incidence angle variation with camber, and (θ) is the camber angle.

Both Lieblein (SP-36 Ch.7, 1965) and Hearsey (1970), using corrections based on inlet relative Mach number, adjusted the minimum-loss incidence **(i*)** described in Equation 2.13 to apply to a 3-D cascade. The difference between the Lieblein and Hearsey modifications of **(i*)** was that they used different empiricism due to their differing data sets.

The equation in the open literature most commonly used to calculate minimum-loss deviation angle is shown in Equation 2.14.

$$\delta^* = m_c \theta / \sigma^b \qquad \textbf{(2.14)}$$

In Equation 2.14, (δ^*) is the minimum-loss deviation angle, (m_c) is an empirical relation that is usually a function of exit relative flow angle or stagger angle, (θ) is the blade camber angle, (σ) is the solidity, and (b) is the solidity exponent. The solidity exponent (b) is set to 0.5 in the Carter correlation (Cohen, 1987). Since the Carter correlation was developed for 2-D cascades, Cetin (1987) added empiricism to it in order to adjust the minimum-loss deviation angle calculated by the Carter correlation for 3-D flows. Along with the minimum-loss deviation angle calculated from Equation 2.14, the Hearsey model also included a correction factor due to the velocity ratio.

In the current evaluation, three components are used to model minimum-loss. These components are the profile loss caused by blade boundary layers, the profile loss caused by the mid-span damper, and the shock loss.

In calculating the blade profile loss, all correlations use a technique originally developed by Lieblein (1957), using a diffusion factor which is a function of maximum inlet relative velocity, and inlet and exit relative velocities. The maximum velocity is determined empirically and is a function of circulation, compressibility effects, and blade geometry. Once the momentum thickness is calculated using the diffusion factor, one may apply a compressible mixing loss due to mixing in the wakes. The compressible mixing loss uses that from Stewart (1955). Swan (1961) took the Lieblein diffusion factor and empirically extended it as a function of blade span to apply to a compressor blade. Koch and Smith (1976), who had the most comprehensive model, performed operations similar to Lieblein, but better accounted for viscosity by including Reynolds number and surface friction effects. The Hearsey model differed from Lieblein in that it contained a correction for profile loss at inlet relative Mach numbers greater than the critical inlet relative Mach number.

The basis for most modern shock loss models is that of Miller-Hartmann-Lewis (1961). Their model, which can be used to calculate minimum-loss shock loss, is described using Figure 2.7.

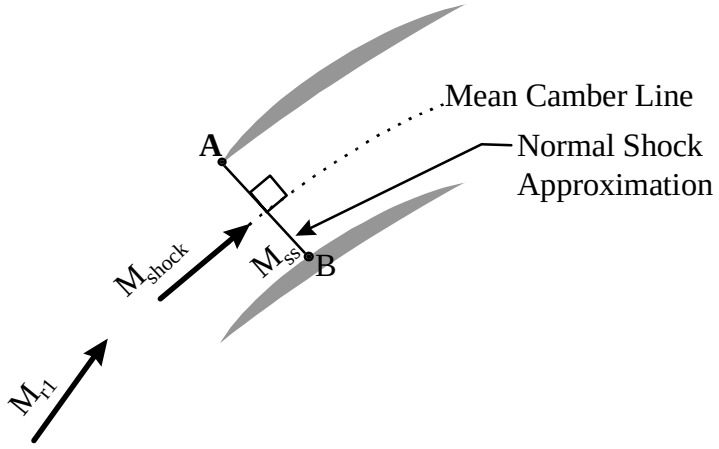

Figure 2.7 Schematic of Miller-Hartmann-Lewis Shock Loss Model

In Figure 2.7, M_{shock} is equal to $(M_{ss} + M_{r1}) / 2$, or the arithmetic average of the suction side and inlet relative Mach numbers. The suction side Mach number at point B can be found by isentropically expanding M_{r1} to the angle tangent to the suction side at point B. Point A is the leading edge of the upper blade in the cascade. Point B on the suction side is found by extending the normal shock perpendicular to the mean camber line until it hits the suction side of the lower blade at Point B.

The Koch and Smith minimum-loss shock loss correlation models two passage shocks, one oblique and one normal, as well as a bow shock at the leading edge. Koch

and Smith arithmetically sum the losses due to each of these shocks to obtain the total shock loss. The bow shock loss is modeled using the entropy rise which is a function of the leading edge radius, solidity, chord, and inlet relative Mach number and flow angle. The normal and oblique shock losses are also functions of inlet relative Mach number and are calculated empirically using curve fits of experimental 2-D cascade data.

Koch and Smith also include a model for losses caused by the presence of a mid-span damper. This model essentially uses a method similar to those used in calculating losses over airfoils and uses the Horner (Koch, 1976) drag coefficient calculation. The drag was assumed to come from two sources: mid-span damper profile drag and interference drag generated between the mid-span damper and the rotor blades. The drag coefficients are then arithmetically summed into a total drag coefficient and then used to calculate entropy generation. Based on the entropy generation, mid-span damper loss may be obtained.

There are essentially three methods of calculating the total off-minimum-loss for transonic flows. The first method calculates a minimum-loss separately then uses the empirical loss equation similar to Equation 2.15.

$$\overline{\omega} = \overline{\omega}_{\min} + a[i - i^*]^2 \qquad \textbf{(2.15)}$$

A form of Equation 2.15 is used by Cetin, Creveling (1968), and Hearsey. This solution method is highly empirical, with the parameter (a) being a function of inlet relative Mach number, flow angle, and blade geometry.

The second method of calculating the total off-minimum-loss sums a constant profile loss to the shock loss that is a function of inlet relative flow angle and relative Mach number. Bloch (1996) is one of the most fundamentally based models available, and includes a bow shock as well as a passage shock due to a combination of normal and oblique shocks within the blade passage. The Bloch model is based on actual shock structures found in 2-D cascade Schlieren photographs of changing shock geometry due to varying back pressure over the started choke regime and varying the inlet angle over

the unstarted regime at constant Mach number. Konnig (1996 Pt. II) used an oblique and a normal passage shock to model the shock loss in the blades, and a method similar to Miller-Hartmann-Lewis to find the Mach number immediately upstream of the first oblique shock. Konnig then determined empirically a fictitious area ratio between the areas at the positions of the oblique and normal shocks, and used nozzle theory in order to calculate the Mach number immediately upstream of the normal shock.

The third method of calculating the total off-minimum-loss is very similar to the method used to calculate minimum-loss profile loss. This time, however, diffusion factor is corrected away from minimum-loss incidence. Lieblein (1957), Swan (1961), and Konnig (1996, Pt. I) use this method of prediction, which is only applicable for subsonic inlet relative Mach numbers.

Off-minimum-loss deviation angle prediction is performed almost completely empirically. The standard method is to use the minimum-loss deviation angle prediction as shown in Equation 2.16.

$$\delta = \delta^* + a(i - i^*)^2 + b(i - i^*) + c \qquad \textbf{(2.16)}$$

In Equation 2.16, (δ) is the off-minimum-loss deviation angle, (δ^*) is the minimum-loss deviation angle, and (a), (b), and (c) are empirically determined constants. All correlations used in the current evaluation, Creveling, Lieblein (SP-36 Ch. 6, 1965), Hearsey, and Howell (1947) used a variation of this method. Because the Lieblein correlation was originally developed for a 2-D cascade, his method was modified by Jansen and Moffatt (1967) to fit a 3-D annulus.

Chapter 3.0 Approach

The objective of the present research is to evaluate the existing loss and deviation models at the meanline by comparing them to experimental data obtained for a rotor and a stage. A study was conducted of the compressible meanline code (CMLC) developed by Hale at Arnold Engineering Development Center (AEDC). The initial objectives were to comprehend how the code functioned and to prepare it for the correlation study. This was accomplished by reviewing the theory in the CMLC for completeness and correctness. A review of the CMLC FORTRAN coding was conducted and modifications were performed which made the codes more user friendly and expandable. The CMLC was also updated to handle additional input situations and compute source terms. Lastly, test cases were executed in order to verify the code with regard to accuracy and robustness.

3.1 CMLC Theory

The CMLC is a compressible, 1-D, steady-state, stage-by-stage characteristics solver. It also has the capability to become a pseudo 2-D solver if the positions of streamtubes and their respective inputs are known. The CMLC code assumes a perfect gas with constant properties, inviscid flow and adiabatic walls upstream and downstream of the blades, and constant rothalpy within a streamtube through the blades. The blade rows are replaced by semi-actuator disks, and all of the losses and inefficiencies that are manifested in the span of the blade are modeled by loss and deviation correlations. Semi-actuator disk theory replaces the blade geometry with an externally imposed discontinuity in the flow properties over the axial spacing of the bladed region (Hale, 1996).

Below is a listing of the equations and methodology used by the CMLC. Given the relative inlet Mach number M_1, the swirl angle α_1, static pressure P_1, static temperature T_1, compressor rotational speed Ω, streamline radii r_1 and r_2 at the inlet and exit of the blade, the 3-D streamtube contraction ratio MVDR, and loss ($\overline{\omega}_{3D}$) and deviation (δ), all thermodynamic and fluid flowfield properties may be obtained. Below is a list of some compressible flow relations that the CMLC uses throughout its progression.

$$\frac{P}{P_t} = \left(1 + \frac{(\gamma - 1)}{2} M^2\right)^{\left(\frac{-\gamma}{\gamma - 1}\right)} \quad \textbf{(3.1)}$$

$$\frac{T}{T_t} = \left(1 + \frac{(\gamma - 1)}{2} M^2\right)^{-1} \quad \textbf{(3.2)}$$

$$V = M \bullet a = M\sqrt{\gamma RT} \quad \textbf{(3.3)}$$

Equations 3.1 and 3.2 can be used to go from the static to total thermodynamic states or vice versa. Figure 3.1 illustrates the process of changing reference frames between relative and absolute.

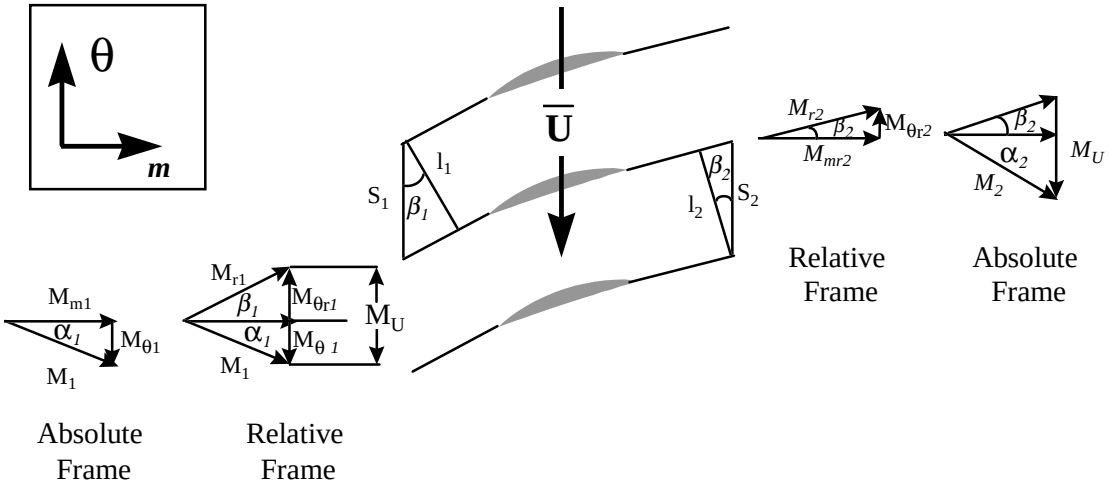

Figure 3.1 Absolute and Relative Reference Frames for an Axial-flow Compressor Rotor

Using the Equations 3.4 through 3.11 below one can solve for M_{r1}.

$$U = r(\Omega) \quad \textbf{(3.4)}$$

$$M_{\Theta 1} = M_1 \bullet \mathrm{Sin}(\alpha_1) \quad \textbf{(3.5)}$$

$$M_{m1} = M_1 \bullet \mathrm{Cos}(\alpha_1) \quad \textbf{(3.6)}$$

$$M_{mr1} = M_{m1} \quad \textbf{(3.7)}$$

$$\overline{M_{\Theta r1}} = \overline{M_{\Theta 1}} - \frac{\overline{U_1}}{\sqrt{\gamma R T_1}} \tag{3.8}$$

$$\beta_1 = \mathrm{Tan}^{-1}\left(\frac{M_{\Theta r1}}{M_{mr1}}\right) \tag{3.9}$$

$$i = \beta_1 - \beta_1' \tag{3.10}$$

$$M_{r1} = \sqrt{M_{mr1}^2 + M_{\Theta r1}^2} \tag{3.11}$$

Once M_{r1} has been determined, the program will use the compressible flow relations to solve for P_{tr1} and T_{tr1}. In addition, with knowledge of M_{r1}, the non-dimensionalized mass flow function MFF_{r1} can be resolved using Equation 3.12.

$$\mathrm{MFF} = \frac{\dot{m}\sqrt{T_t}}{P_t A} = M\sqrt{\frac{\gamma}{R}}\left[\frac{1}{1+\frac{\gamma-1}{2}M^2}\right]^{\frac{\gamma+1}{2(\gamma-1)}} \tag{3.12}$$

Note that the MFF is a function of Mach number M and the ratio of specific heats γ. MFF_{r2} is solved for using Equation 3.13

$$\left(\frac{\dot{m}\sqrt{T_{tr}}}{P_{tr}A}\right)_2 = \left(\frac{\dot{m}\sqrt{T_{tr}}}{P_{tr}A}\right)_1 \frac{\dot{m}_2}{\dot{m}_1}\sqrt{\frac{T_{tr2}}{T_{tr1}}}\left(\frac{P_{tr1}}{P_{tr2}}\right)\left(\frac{A_1}{A_2}\right) \tag{3.13}$$

where $\sqrt{\frac{T_{tr2}}{T_{tr1}}}$ =1 by assuming constant rothalpy, $\frac{\dot{m}_2}{\dot{m}_1}$ =1 from continuity, and $\left(\frac{A_1}{A_2}\right)$ is the streamtube contraction ratio of the cross-sectional areas which are perpendicular to the relative flow, determined from Equation 3.14.

$$\left(\frac{A_1}{A_2}\right) = \mathrm{MVDR}\left(\frac{\mathrm{Cos}(\beta_1)}{\mathrm{Cos}(\beta_2)}\right) \tag{3.14}$$

The relative total pressure ratio $\left(\frac{P_{tr2}}{P_{tr1}}\right)$ is found by solving Equations (3.15), (2.4), and (3.16).

$$\left(\frac{P_{tr2}}{P_{tr1}}\right) = \left(\frac{P_{tr2}}{P_{tr2ideal}}\right)\left(\frac{P_{tr2ideal}}{P_{tr1}}\right) \tag{3.15}$$

$$\frac{P_{tr2\ ideal}}{P_{tr1}} = \left\{1 + \frac{\gamma-1}{2} * \frac{(\Omega r_2)^2}{\gamma R T_{tr1}} [1 - (r_1/r_2)^2] \right\}^{\gamma/(\gamma-1)} \quad \textbf{(2.4)}$$

$$\frac{P_{tr2}}{P_{tr2ideal}} = 1 - \bar{\omega}\left(1 - \frac{P_1}{P_{tr1}}\right) \quad \textbf{(3.16)}$$

After MFF_{r2} is found, M_{r2} can be determined by numerically solving Equation 3.12. Because Equation 3.12 can yield both a supersonic and subsonic solution, the user must specify if the relative exit flow is subsonic or supersonic. The relative exit flow angle β_2 is determined directly from Equation 3.17

$$\beta_2 = \beta_2' + \delta \quad \textbf{(3.17)}$$

It must be stated that the loss $\bar{\omega}$ and deviation angle δ are either directly entered or must be determined from correlations. MVDR is also a required input that can be determined in an SLCC or can be converged upon if a different exit flow condition is specified.

P_{tr2} can be solved for using Equation 3.15, assuming $T_{tr2} = T_{tr1}$. Then the static exit state with P_2 and T_2 can be solved for in Equations 3.1 and 3.2 using M_{r2} as the Mach number. With M_{r2} and β_2 known, the exit Mach number in the absolute frame can found using the geometric relation as pertains to Figure 3.1. Then the absolute thermodynamic states and fluid velocities are determined once again by solving the compressible flow relations stated earlier.

3.1.1 Structure and Input

Figure 3.2 is a flowchart of the CMLC, which begins with an input file containing all necessary geometry, gas properties, and flowfield information required to solve the stage characteristics.

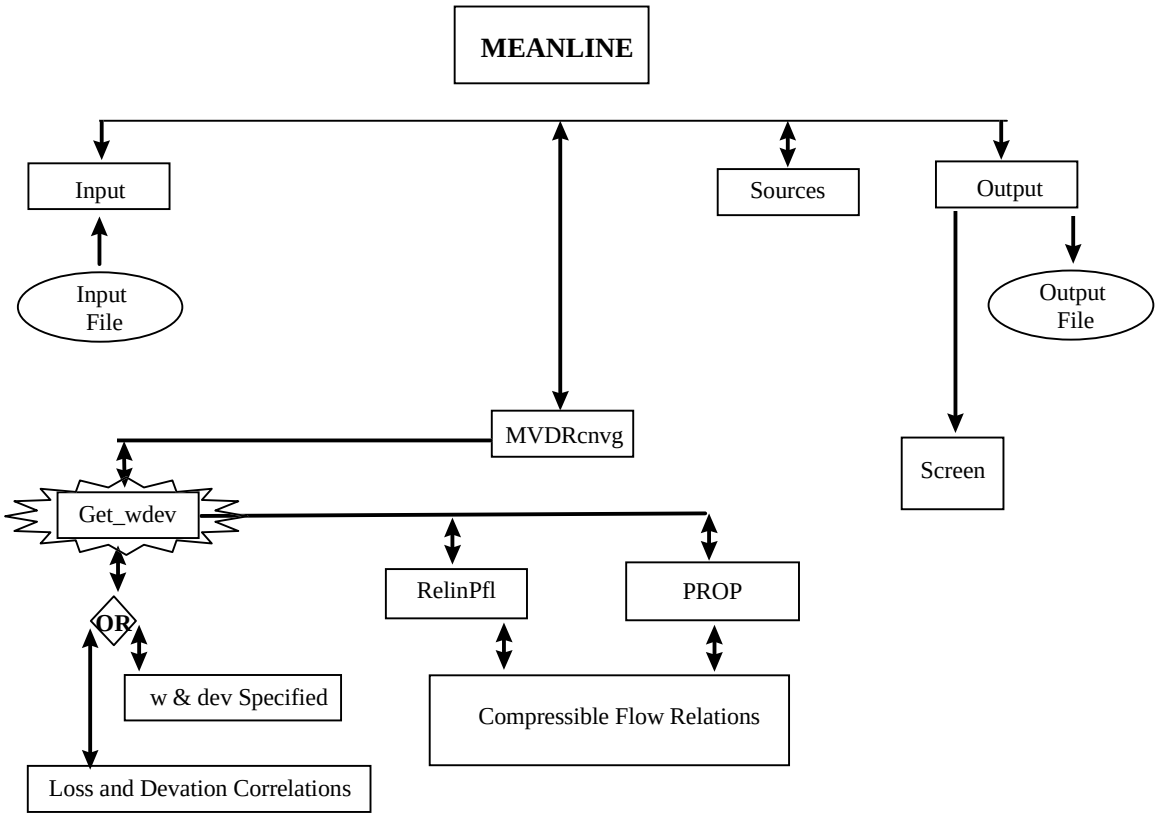

Figure 3.2 Flow chart of CMLC

If MVDR is not specified the subroutine *MVDRcnvg* is used to iterate and converge on the MVDR assuming that an exit flowfield quantity is given. Next, subroutine *Get_wdev* is called which will call the loss and deviation angle correlations unless they are previously specified. Once MVDR, loss, and deviation angle are known, the program will call subroutine *RelinPfl* which will compute the relative input properties using velocity triangles and the compressible flow relations. Then subroutine *PROP* calculates the relative and absolute exit flow properties by utilizing the compressible flow relations and velocity triangles. After all downstream information has been determined, the subroutine *Sources* calculates power and force requirements. Finally, the subroutine *Output* .writes information to both the screen and a file.

3.2 Correlation Categories

Models from the literature review were categorized into five groups of predictions which were minimum-loss incidence, minimum-loss, off-minimum-loss, minimum-loss deviation, and off-minimum-loss deviation. These five groups were then divided into subcategories. In minimum-loss prediction, the subcategories were shock loss and profile loss. For off-minimum-loss prediction, the subcategories were shock loss, profile loss, and total loss. The mid-span damper loss prediction was included in both minimum-loss and off-minimum-loss predictions. Table 3.1 lists the various correlations according to their specific categories.

Table 3.1 Categories of Correlations

Minimum-Loss Incidence (i^*)	
SP 36 (Lieblein)	CPAC (Hearsey)

(A)

Minimum-Loss Deviation (δ^*)		
CPAC (Hearsey)	Carter	Carter Modified (Cetin)

(B)

Minimum-Loss ($\overline{\omega}^*_{min}$)						
Shock Loss		**Profile Loss**				**Damper Loss**
Hartmann Lewis Miller	Koch Smith	Lieblein	Swan	CPAC (Hearsey)	Koch Smith	Koch Smith

(C)

Off-Minimum-Loss ($\bar{\omega}$)								
Shock Loss		**Profile Loss**			**Total Loss**			**Damper Loss**
Bloch	Könnig	Lieblein	Swan	Könnig	CPAC (Hearsey)	Creveling	AGARD (Cetin)	Koch Smith

(D)

Off-Minimum-Loss Deviation (δ^*)			
Howell	Lieblein Modified (Jansen & Moffatt)	CPAC (Hearsey)	Creveling

(E)

3.3 Implementation of Loss Models into CMLC

Inputs necessary to run the CMLC included blade metal angles β'_i, stagger angles ξ, solidity σ, inlet and exit radii r_1 and r_2, machine speed Ω, MVDR, LER, TER, c, *a*/c, t_{max}/c, and flow conditions M_1, inlet total pressure P_{t1}, and inlet total temperature T_{t1}. In order to circumvent the input process, the geometry and the inlet conditions were hardcoded into separate subroutines for NASA Rotor 1-B, NASA Rotor 35, and NASA Stator 35. Correlations were created to accept either SI or English units. Therefore, the input data had to be converted into the required units before and after the particular correlation subroutine was run.

Programming the correlations was a difficult task due to the fact that they were obtained from technical papers as opposed to borrowing subroutines developed by the authors. This required complete understanding of each author's logic. Several authors used different nomenclature, units, and sign convention. These authors also placed certain restrictions on their correlations while other authors modified previous correlations to accommodate their own needs. With such a large number of equations,

restrictions, units, nomenclature, and sign conventions, it was not uncommon to stumble upon errors and abuse of theory.

Most of the correlations utilized graphs in order to demonstrate relationships between variables. The data from each of these graphs was converted to either a curve fit or a series of curve fits. Linear interpolation was used as necessary when data fell between two data points.

Bloch (1996) created an off-design shock loss model for a linear 2-D cascade which uses the cascade geometry profiles for the suction and pressure sides of the blade, the solidity (σ), and the LER and TER. The only flow condition required for input was the relative inlet Mach number (M_{r1}). The Bloch model was created in the C programming language, and in addition to the main theory, contained methods of grid generation and convergence. Therefore, it was decided not to recode the Bloch model in FORTRAN but to modify its existing code to accept different inputs. The Bloch program could then be used as an external program that could be called on from the FORTRAN-based CMLC.

The FORTRAN subroutine *Bloch* utilizes its RUNQQ command which calls the executable and contains the necessary inputs such as the names and locations of the geometry input files as well as the relative inlet Mach number (M_{r1}). After the Bloch program was executed and had written its results to a file, the results were gathered in the FORTRAN subroutine and the useful data was saved.

One major problem existed in the implementation of the Bloch model in that it demonstrated that a 2-D cascade chokes at a unique incidence, also called the minimum-loss incidence, implying that the loss versus incidence curve becomes vertical. This phenomenon was not demonstrated from the experimental data for the 3-D annular cascade Rotor 1-B. The Rotor 1-B experimental data illustrated that at incidences less than that of minimum-loss the loss versus incidence curve was not vertical. In order to

model this experimental data correctly, a linear interpolation was performed for that region of the data and a slope was incorporated on the choke line.

3.4 Modeling Decisions

The two experimental configurations available for modeling were NASA Rotor 1-B and NASA Stage 35 (see Appendices A and B, respectively). Rotor 1-B was a transonic rotor which had a mid-span damper. Experimental data was available for Rotor 1-B for its 100%, 90%, 70%, and 50% speed lines, with each speed line consisting of six to eight data points at various mass flow rates. At the meanline, the Rotor 1-B 100% and 90% speed lines corresponded to supersonic relative inlet conditions and the 70% and 50% speed lines corresponded to subsonic relative inlet conditions. Stage 35 consisted of a rotor (Rotor 35), and a stator (Stator 35) which was exposed to the exit flow of Rotor 35 in a stationary frame of reference. Rotor 35 information consisted of three data sets, which were the 100%, 90%, and 70% speed lines, with each speed line containing five data points at various mass flow rates.

Two-dimensional cascade data is obtained using a constant inlet relative Mach number with a varying angle of attack in order to create the loss curve. To obtain an analogous loss curve for constant inlet relative Mach number would be extremely difficult for a 3-D annular cascade. It would require varying the rotor speed and throttle simultaneously until the inlet relative Mach number matched that for the previous test condition. Therefore, 3-D rotor data is obtained by opening the throttle of the compressor, which increases mass flow, inlet relative Mach number, and subsequently decreases the angle of attack. A difference arises due to the fact that off-minimum-loss loss curves created in 2-D cascades use a constant inlet relative Mach number, while off-minimum-loss curves in 3-D cascades occur over a range of inlet relative Mach numbers. This creates a problem in comparing 2-D to 3-D loss curves because only one point of each 2-D constant Mach number loss curve can be compared to experimental 3-D data.

Two techniques are available which allow direct comparison between experimental and simulated off-minimum-loss curves. The first method requires the user to predict a minimum-loss point in order to solve for the off-minimum-loss points on the same inlet relative Mach number loss curve (see Figure 3.3).

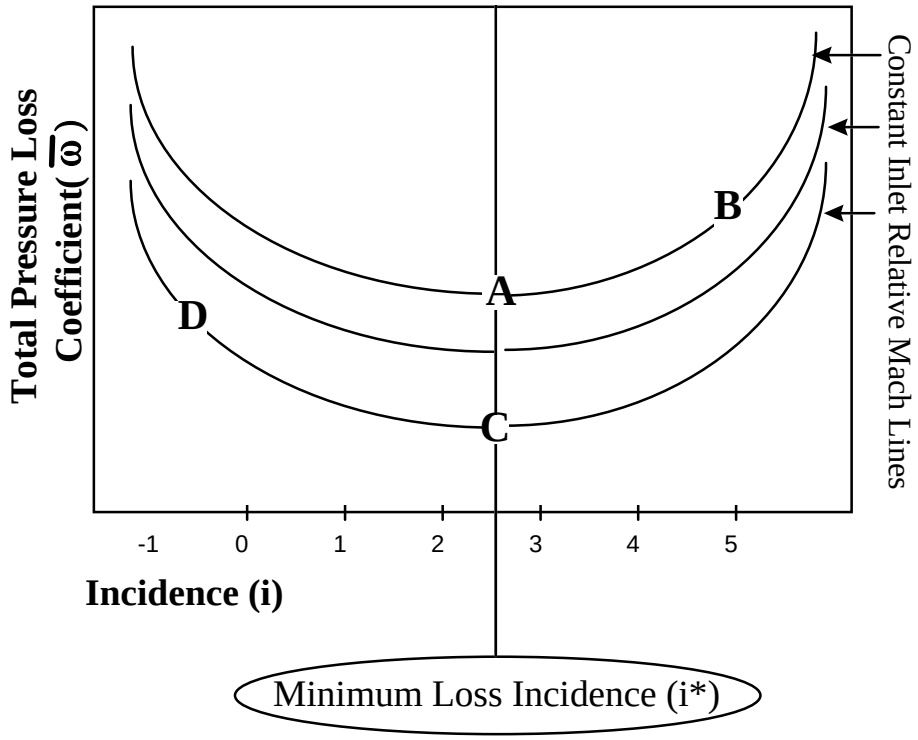

Figure 3.3 Total Pressure Loss Versus Incidence Angle for 2-D Cascade

In Figure 3.3, points A and C are selected as the minimum-loss points for each loss curve, then correlations are used to find the off-minimum-loss points B and D corresponding to points A and C on their respective loss curves. The advantage of this first method is that it uses the same relative inlet Mach number to calculate off-minimum-loss points. The disadvantages are that one can only compare one point of each loss curve for a constant relative inlet Mach number and that one cannot use the experimental loss found but must predict their own for each loss curve.

The second method assumes points A and C have the same experimentally determined minimum-loss point for a given speed line (see Figure 3.4).

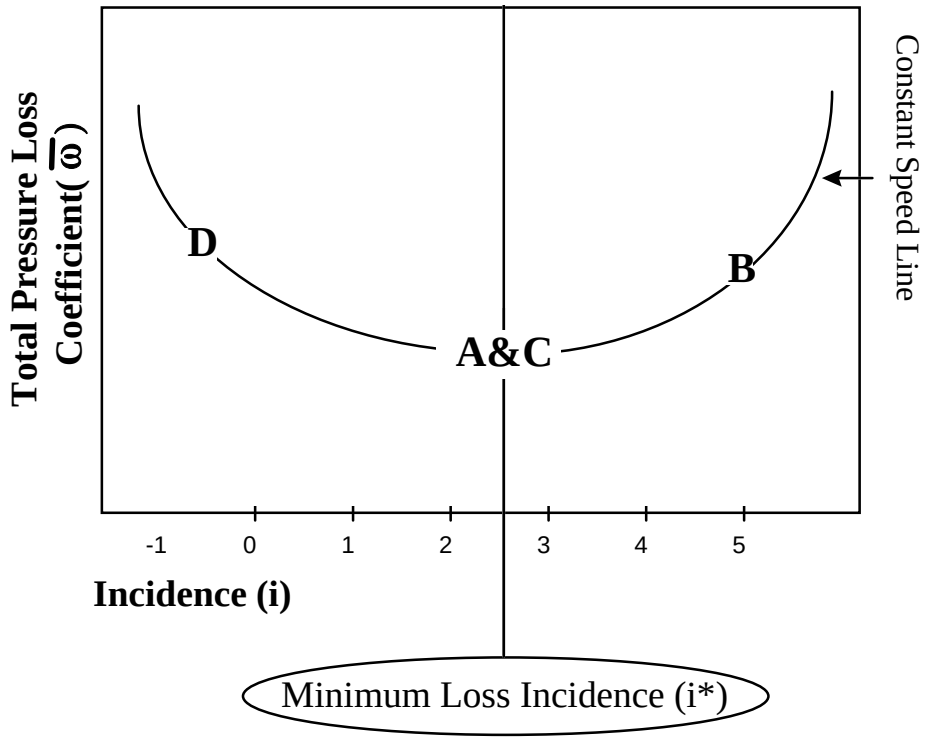

Figure 3.4 Total Pressure Loss Versus Incidence Angle for 3-D Annular Cascade

The advantage of this second method is that one can use experimental results for the minimum-loss point as the minimum-loss point for off-minimum-loss curve prediction. The disadvantage of the second method is that the inlet relative Mach numbers may be slightly different than those for the minimum-loss points one is trying to evaluate.

For Rotor 1-B, the Koch and Smith model predicted a design profile loss of approximately 0.026 to 0.036 between inlet relative Mach numbers of 0.55 to 1.18. For Rotor 35, the Koch and Smith model predicted a design profile loss of approximately 0.016 to 0.021 between inlet relative Mach numbers of 0.94 to 1.4.

As a result, the Koch and Smith model showed that the inlet relative Mach number does not have a significant influence on the design profile loss. Therefore, the second method of comparing experimental to simulated results was selected in order to evaluate off-minimum-loss correlations for subsonic inlet relative Mach numbers. Conversely, shock losses were found to be a strong function of inlet relative Mach number. Therefore, the first method of comparing experimental and simulated results was selected in order to evaluate off-minimum-loss correlations for supersonic inlet relative Mach numbers.

3.5 Detailed Plan

Accurate testing of the correlations required experimental data for a stage. Sets of data were available for both a rotor (Rotor 1-B) and a stage (Stage 35). These data acted as control references to validate the results of the correlations. The Hearsey and Cetin correlations were coded and prepared for the CMLC and were the first correlations tested in the CMLC. After running the full range of speeds and operating conditions, the results were documented and compared with experimental data from Rotor 1-B and Stage 35. Next, an investigation of other existing correlations in the open literature was conducted. The correlations which fit the conditions of transonic axial compressors were coded and tested at the meanline. After all CMLC testing was completed, the correlation results were compared and the optimum loss and deviation correlations were determined for each speed and inlet flow condition.

Chapter 4.0 Results and Discussion

In this chapter, the various minimum-loss and off-minimum-loss correlations will be evaluated against experimental data for a rotor (Rotor 1-B) and a stage (Stage 35). Experiment information for Rotor 1-B and Stage 35 can be found in Appendices A and Appendix B, respectively.

First, the point of minimum-loss was evaluated. In order to have an accurate minimum-loss point, one must predict the minimum-loss incidence, the minimum-loss, and the minimum-loss deviation angle. A method for reducing the data was required in order to test accurately the off-minimum-loss case. Then, the points other than minimum-loss were evaluated. It was assumed for Rotor 1-B and Stage 35 that in order to provide an accurate analysis, loss had to be predicted to within $\pm$ 0.01 and deviation had to be predicted to within $\pm$ 1°. This would result in a difference in total pressure rise in the absolute frame of reference to within 3% and an accuracy in efficiency to within 2%.

4.1 Data Reduction Methods

Figure 4.1 depicts a loss curve for a transonic compressor using loss as the ordinate and incidence as the abscissa.

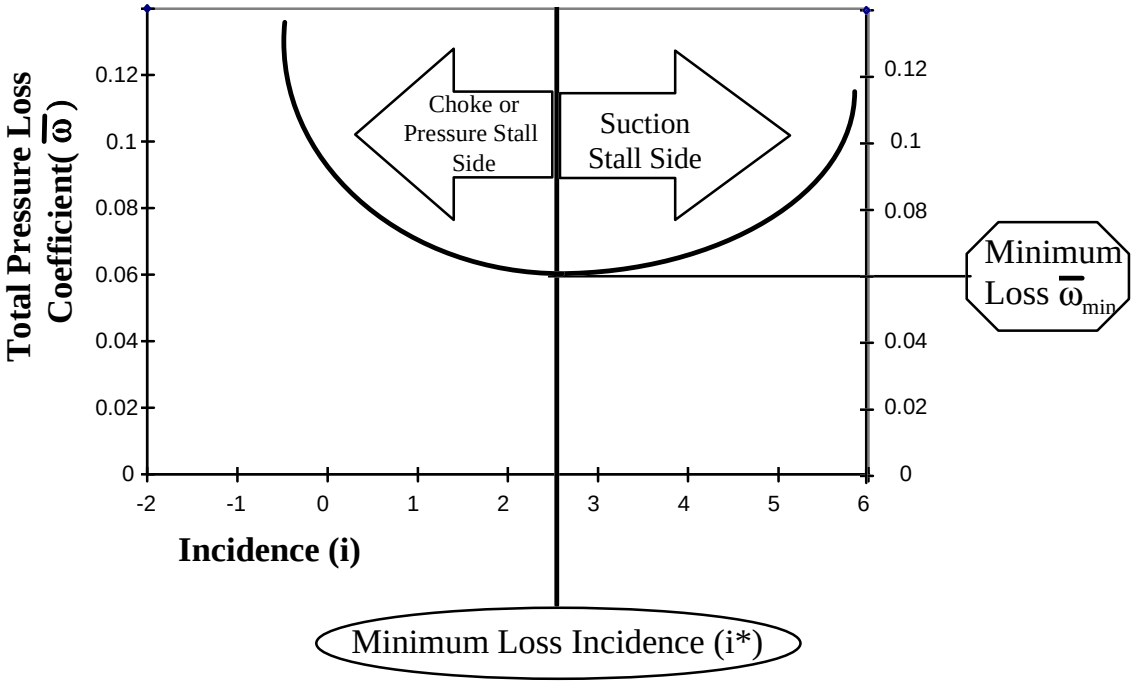

Figure 4.1 Division of Loss Curve into Choked and Stalled Regions

The loss curve refers to the curve created by varying the flow incidence to the compressor blade and measuring the resulting non-dimensionalized total pressure loss coefficient as described in Section 2.2. The region to the right of the minimum-loss point where incidence is greater than the minimum-loss incidence is referred to as the stall regime because as the incidence is increased the trend on the suction side of the compressor blade is toward stalled flow. Moving in the direction to the left of the minimum-loss incidence, the flow will either choke or will separate from the pressure side of the compressor blade. This region is referred to as the choke regime.

In order to compare effectively the various loss correlations, all of the model results for the loss curves were shifted, or translated, on the loss versus incidence graphs so that the minimum-loss point of each correlation was positioned at the point of minimum-loss for the Rotor 1-B and Stage 35 experiments at a given corrected speed (see Figure 4.2).

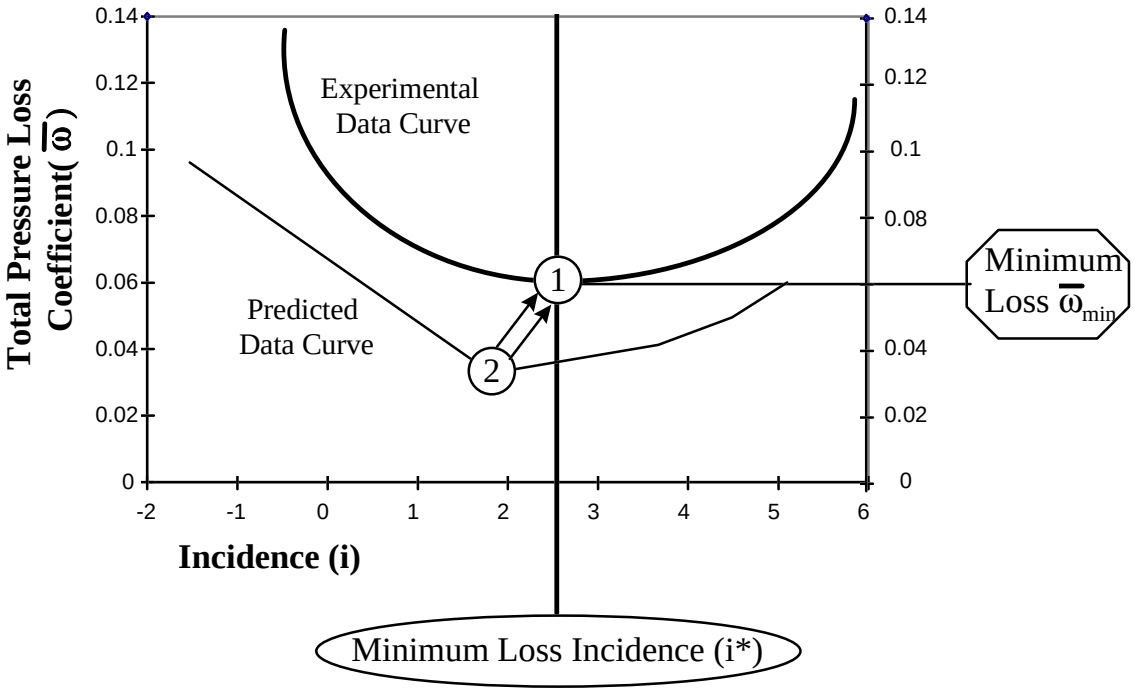

Figure 4.2 Translation of Model Results to Match Experimental Minimum-Loss Points

Figure 4.2 depicts two loss curves, one being an experimental result and the other a data curve predicted using correlations. The minimum-loss point on the experimental result curve is labeled (1) and the minimum-loss point on the predicted curve is labeled (2). The entire predicted data curve is shifted, so that point (2) lies directly on top of point (1). This enables a qualitative analysis of the predicted curve as compared to the experimental curve. A similar method of transformation was used in evaluating the off-minimum-loss deviation angles. This time, however, the experimental deviation angle found at the minimum-loss point was used as the anchor for the off-minimum-loss deviation correlation curves.

A statistical analysis was performed in order to compare the root mean square (RMS), arithmetic mean, and maximum error for each model when compared with Rotor 1-B and Stage 35 experimental results. The error analysis in this project did not attempt to account for the error in the experimental data, only the difference between the experimental and predicted values.

For this analysis, the errors were defined as follows:

$$\mathbf{Error} = \left|\mathbf{x}_i - \mathbf{y}_i\right| \tag{4.1}$$

$$\mathbf{Error}_{\mathbf{Mean}} = \frac{\sum \left|\mathbf{x}_i - \mathbf{y}_i\right|}{\mathbf{N}} \tag{4.2}$$

$$\mathbf{Error}_{\mathbf{RMS}} = \sqrt{\frac{\left[\sum \left(\mathbf{x}_i - \mathbf{y}_i\right)^2\right]}{\mathbf{N}}} \tag{4.3}$$

In Equations 4.1 to 4.3, x represents the experimental data and y represents the predicted values. The subscript i represents an individual data point and N is the number of data points in the analysis. The maximum error between experimental and predicted values was also calculated. Bar graphs were created in order to visualize the results. Figure 4.3 shows a bar graph of loss prediction errors for Rotor 1-B at 100% speed.

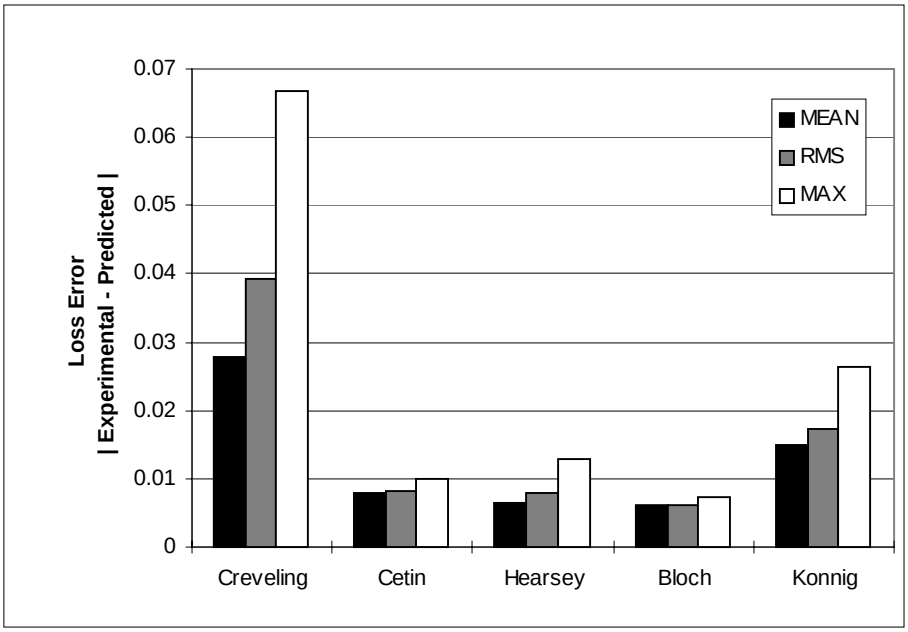

Figure 4.3 Typical Bar Graph of Loss Prediction Errors

The RMS error between experiment and prediction was chosen as the optimum method of evaluating the off-minimum-loss correlations. This was because larger errors are given greater significance in an RMS analysis than in mean error calculations. A mean error was chosen for evaluating the minimum-loss correlations because it was desirable to give equal significance to the different speeds being analyzed.

4.2 Evaluation of Models with NASA Rotor 1-B

4.2.1 Rotor 1-B Minimum-Loss Incidence, Deviation Angle, and Loss Prediction

The foundation of building accurate loss and deviation angles is predicting accurate minimum-loss incidence. It is this point where the loss curves are centered. Table 4.1 describes how well the minimum-loss incidence was predicted by the Lieblein correlation in NASA SP-36 and by a similar method used by Hearsey in CPAC.

Table 4.1 Rotor 1-B Evaluation of Minimum-Loss Incidence Prediction

% Speeds	Experiment (deg)	NASA SP-36 (deg)	Hearsey (deg)
100	5.04	12.02	4.69
90	5.27	12.02	4.61
70	6.03	7.97	5.42
50	8.7	4.02	4.68
Mean Error		**5.09**	**1.41**

For Rotor 1-B minimum-loss incidence, the Hearsey model clearly provided a better prediction than the Lieblein correlation. For rotor speeds of 100%, 90%, and 70%, the Hearsey model predicted values well within 1° of the data which was experimentally measured and converted to the relative frame of reference. These results were extremely accurate considering that the probe in Stage 35 could measure flow angles to an accuracy of ±1°. For Rotor 1-B, the correlation in NASA SP-36 displayed almost four times the mean error than did the Hearsey model.

The next important parameter which required prediction was the minimum-loss deviation. This parameter was necessary for predicting off-minimum-loss deviation, and some minimum-loss correlations required this information as well. Table 4.2 shows the results of Hearsey model, two different uses of the Carter correlations, and modifications of these correlations which were performed by Cetin. The difference between the two Carter correlations is that one is a function of the exit blade metal angle and the other is a function of blade stagger angle. These two blade parameters are related and their relationship varies according to blade shape.

Table 4.2 Rotor 1-B Evaluation of Minimum-Loss Deviation Angle Prediction

% Speed	Experimental (deg)	Hearsey (deg)	Carter $f(B_2')$ (deg)	Modified by Cetin (deg)	Carter f(stagger) (deg)	Modified by Cetin (deg)
100	6.26	1.96	2.02	4.18	2.00	4.13
90	4.9	1.67	2.02	4.18	2.00	4.13
70	5.16	1.83	2.02	4.18	2.00	4.13
50	5.36	1.79	2.02	4.18	2.00	4.13
	Mean Error	**3.61**	**3.40**	**1.24**	**3.42**	**1.29**

For Rotor 1-B minimum-loss deviation angle, both of the Carter correlations modified by Cetin predicted values with mean differences of 1.24° and 1.29° from the data which was experimentally measured and converted to the relative frame of reference. Again, this was considered accurate in relation to the experiment, as the probes were only capable of measuring angles within the accuracy of ± 1°. However, a 1° difference in deviation can produce up to a 3% difference in the absolute exit total pressure and a 2% difference in efficiency. As can be seen in Table 4.2, the Hearsey model and both unmodified Carter correlations produced errors in minimum-loss deviation angle of over 3°.

Evaluating the minimum-loss prediction was the next important step prior to calculating accurate off-minimum-loss predictions. This task was extremely difficult, as only the total loss was determined experimentally as opposed to the loss produced by individual mechanisms. For this reason, there was no means for quantifying with confidence the loss predicted by individual mechanisms, only the total loss obtained by superposing all mechanisms involved. As a result, much of the minimum-loss evaluation was based on previous findings and soundness of theory involved.

Again, Table 3.1 (C) shows a list of correlations used in minimum loss prediction.

Table 3.1(C) Categories of Correlations

Minimum-Loss $(\overline{\omega}^*_{min})$						
Shock Loss		**Profile Loss**				**Damper Loss**
Hartmann Lewis Miller	Koch Smith	Lieblein	Swan	CPAC (Hearsey)	Koch Smith	Koch Smith

There are two predominate sources of loss at the meanline in a transonic blade row: losses due to shocks and losses due to boundary layers. At the meanline, boundary layers are present on the blades and the mid-span damper, and for modeling purposes the boundary layers on the two machine components were considered separate sources of loss. All of the losses generated by each loss mechanism were superposed to obtain a total loss. Consequently, if one correlation was chosen for each loss mechanism, there were eight possible combinations to obtain the total loss.

Table 4.3 contains the eight possible combinations of loss models used to obtain a total minimum-loss prediction.

Table 4.3 Rotor 1-B Evaluation of Minimum-Loss Prediction

Experimental Total Minimum Loss	Koch + Koch + Koch	Koch + Miller + Koch	Lieblein + Koch + Koch	Lieblein + Miller + Koch	Swan + Koch + Koch	Swan + Miller + Koch	Hearsey + Koch + Koch	Hearsey + Miller + Koch
0.097	0.101	0.125	0.147	0.171	0.198	0.222	0.117	0.141
0.044	0.067	0.087	0.092	0.112	0.126	0.146	0.089	0.109
0.049	0.042	0.042	0.052	0.052	0.064	0.064	0.069	0.069
0.046	0.036	0.036	0.042	0.042	0.054	0.054	0.063	0.063
MEAN ERROR	**0.011**	**0.022**	**0.026**	**0.037**	**0.051**	**0.062**	**0.025**	**0.036**

In Table 4.3, the titles for the predictions contain the names of the blade profile loss model + shock loss model + damper loss model. The second, third, fourth and fifth rows of the table contain the total minimum-loss results from Rotor 1-B's 100%, 90%, 70%, and 50% corrected speed lines, respectively. It should be stated that the 100% and 90% corrected speed lines contained supersonic relative inlet Mach numbers, and the 70% and 50% corrected speed lines contained subsonic relative inlet Mach numbers. The combination that displayed the smallest mean error over the entire range of corrected speeds was the combination of Koch and Smith shock, blade profile, and damper losses. The mean error between the experimental value of total loss and the Koch and Smith combination was .011. Results were then broken down into those applicable to subsonic and supersonic inlet relative Mach numbers. For the case of supersonic relative inlet Mach numbers, again the Koch and Smith combination of shock, blade profile, and damper losses was clearly superior with an error of .016. However, in the subsonic case the Lieblein correlations for blade profile loss combined with Koch and Smith

correlations for damper loss produced the minimal error at 0.003. This was followed closely by the Koch and Smith combination of blade profile and damper losses, with only 0.009 error. It must be noted that for subsonic inlet relative Mach numbers no shock loss mechanism was included to predict the total loss.

4.2.2 Rotor 1-B Off-Minimum-Loss and Deviation Angle Prediction

As mentioned in the data reduction section, the method used to evaluate the off-minimum-loss predictions illustrates qualitatively the accuracy of the correlations. Figure 4.4 shows the correlations and the experimentally measured values at the 100% speed for Rotor 1-B. The range of relative inlet Mach numbers for this speed was 1.14 to 1.18.

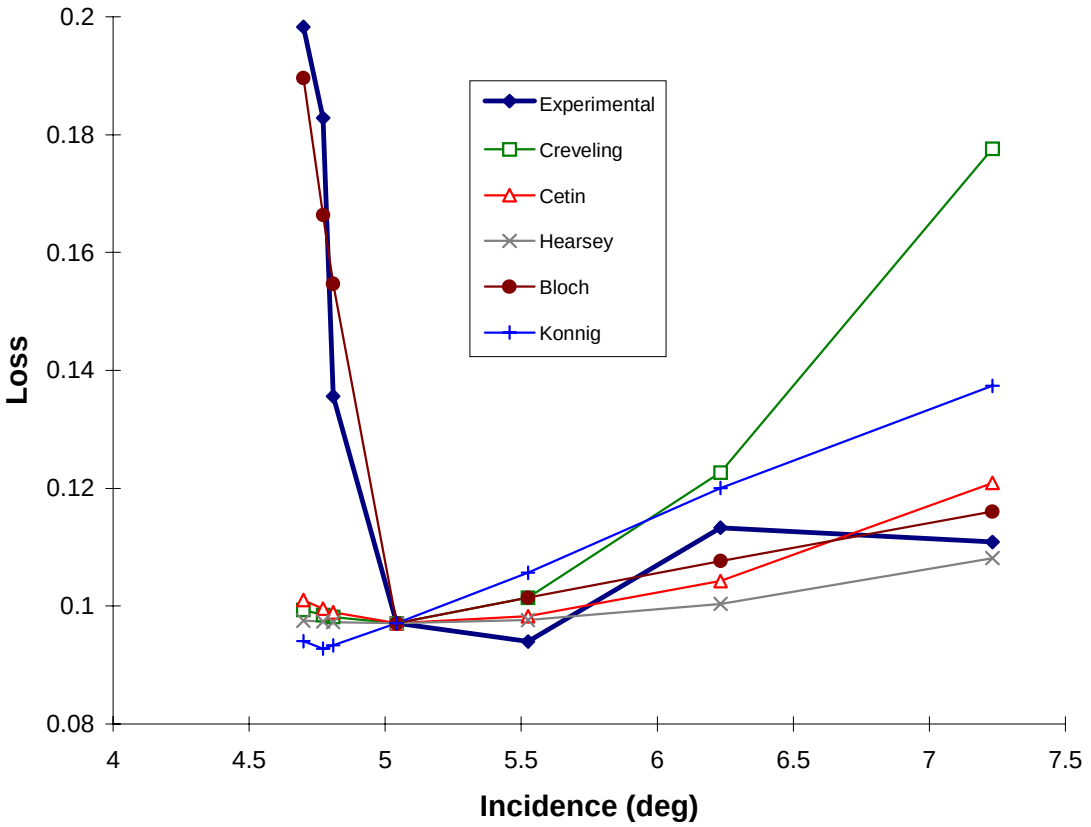

Figure 4.4 Rotor 1-B Loss Curves at 100% Speed

The experimentally measured values were assumed to be the true losses of Rotor 1-B. Every curve is usually centered at the experimentally measured minimum-loss point and its respective incidence. However, note that in Figure 4.4 the curves are centered on

the data point to the left of the minimum-loss point. This is because the author made a logical deduction that the minimum-loss point lies between these two data points and closer to the left point. This hypothesis was supported by experimental data for the 90% speed line, to be shown in Figure 4.5. It was also supported by the correlations which report better qualitative trends on the stall side.

In Figure 4.4, the Bloch model performed best among the models tested for the stalled regime, with an RMS error of only .0061. This result was followed closely by the Hearsey model and the Cetin correlation with RMS errors of only 0.0079 and 0.0082, respectively. Creveling showed the worst agreement with a RMS error of 0.039.

Also in Figure 4.4, none of the correlations tested could predict accurately the losses in the choked regime. The Bloch model formed a vertical line when the cascade choked. Therefore, the Bloch model could not predict loss for incidences less than the minimum-loss incidence. To enable the Bloch model to predict loss in this choked regime, the author added a negatively sloped line which was a linear fit of Rotor 1-B data to the Bloch predicted minimum-loss point. This modification showed the best results, with a RMS error of 0.018. The next best correlation prediction was Cetin, with an RMS error of over 0.06. This magnitude of error in loss prediction would result in approximately a 20% error in total pressure rise in the absolute frame of reference.

Figure 4.5 shows the graph of the off-minimum-loss correlations centered at the experimentally measured minimum-loss point for the Rotor 1-B 90% speed line. The range of relative inlet Mach numbers for this speed was 1.00 to 1.06. The experimentally measured loss data at this speed appears to be very predictable.

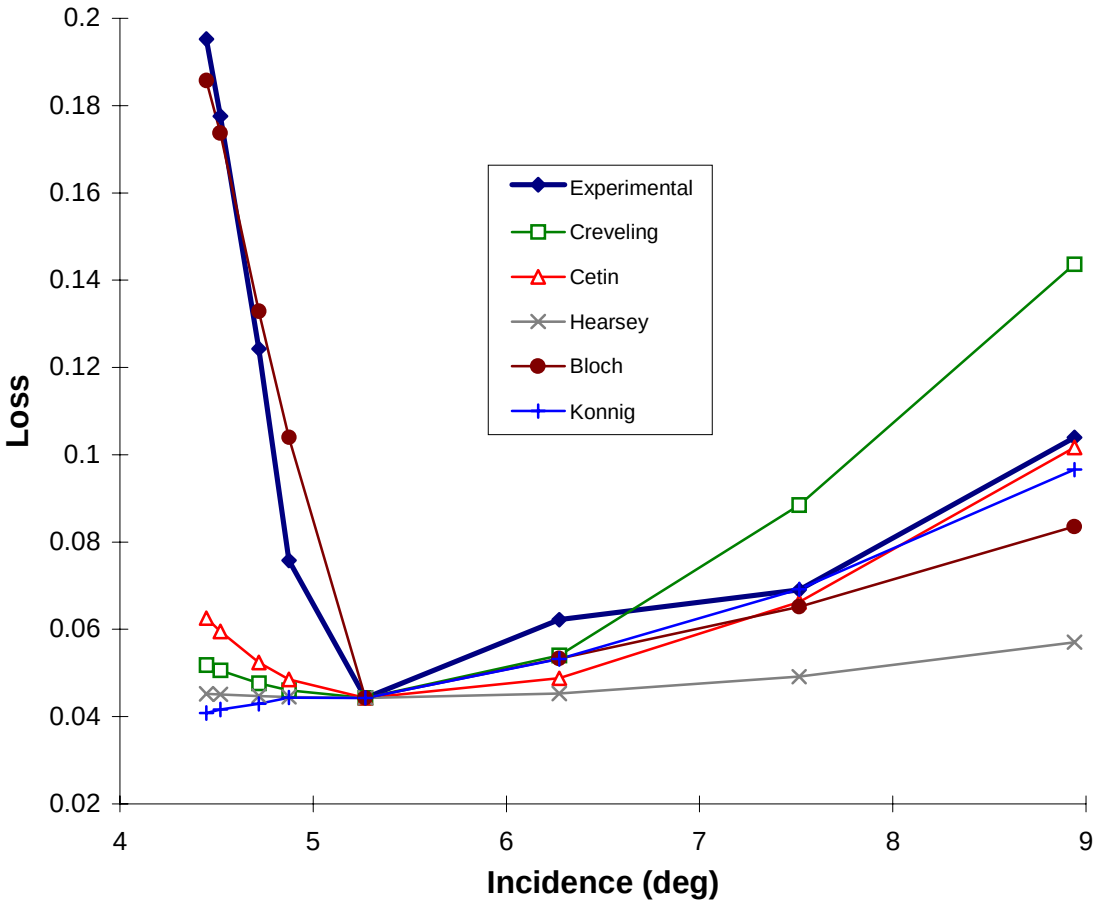

Figure 4.5 Rotor 1-B Loss Curves at 90% Speed

In the stall regime for 90% speed, several correlations performed well in qualitatively predicting loss. The Konnig model had the smallest RMS error of 0.007, followed closely by Cetin and Bloch with RMS errors of 0.008 and 0.013, respectively. However, before the loss curves were translated, the Konnig shock loss correlation predicted loss values much higher than the actual total values. As a consequence, the author is hesitant to recommend the Konnig shock loss model for stall regime predictions.

In the choked regime, again only the modified Bloch model had any success, with an RMS error of 0.016. The next best correlation was again Cetin, with an RMS error of 0.097, almost ten times the acceptable limit.

Figure 4.6 shows the graph of the off-minimum-loss correlations centered at the experimentally measured minimum-loss point for the Rotor 1-B 70% speed line. The range of relative inlet Mach numbers for this speed was 0.74 to 0.81.

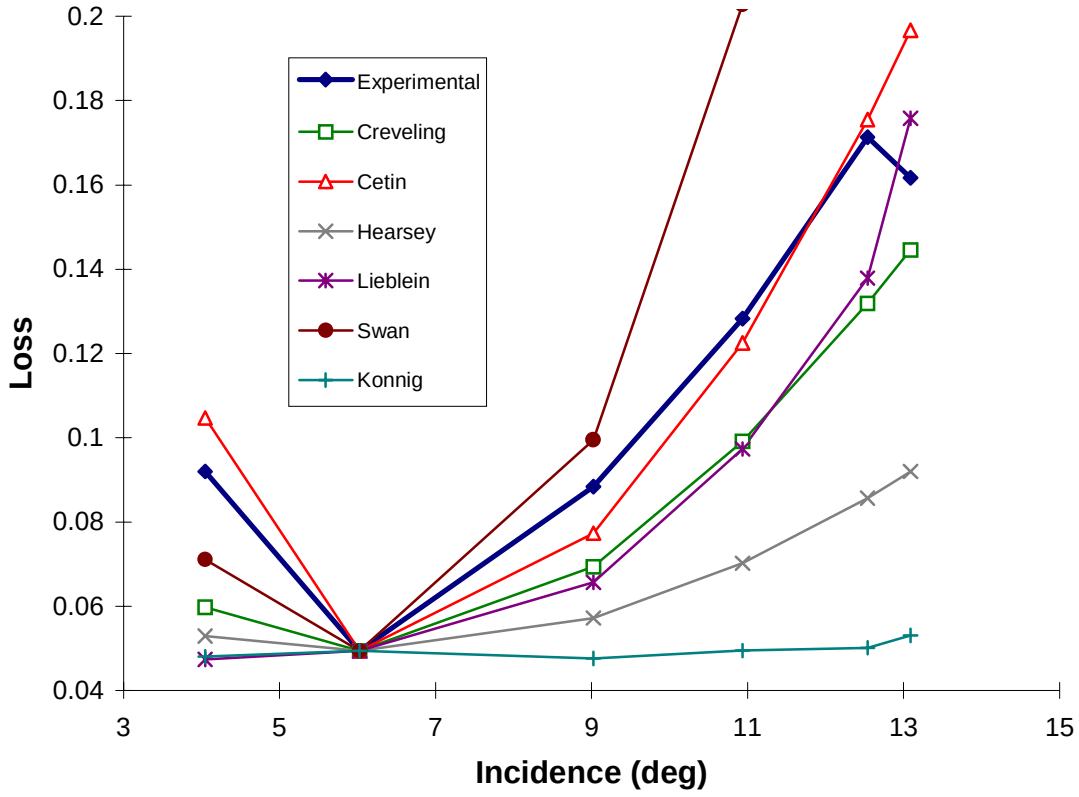

Figure 4.6 Rotor 1-B Loss Curves at 70% Speed

The experimental data for the 70% speed appears well-behaved despite the unexpected decrease in loss at the far right end of its loss curve. This could be an erroneous experimental data point, or may have secondary information that the correlations do not account for. The Cetin correlation gave the least RMS error for both the stall and choke sides at 0.0187 and 0.0127, respectively. However, it should be noted that the choke side had only one experimentally measured data point to be compared against, and more experimental data in this regime is necessary for a better evaluation.

Figure 4.7 depicts the correlation predictions against experimental values for Rotor 1-B at 50% speed. The range of relative inlet Mach numbers for this speed was 0.52 to 0.57.

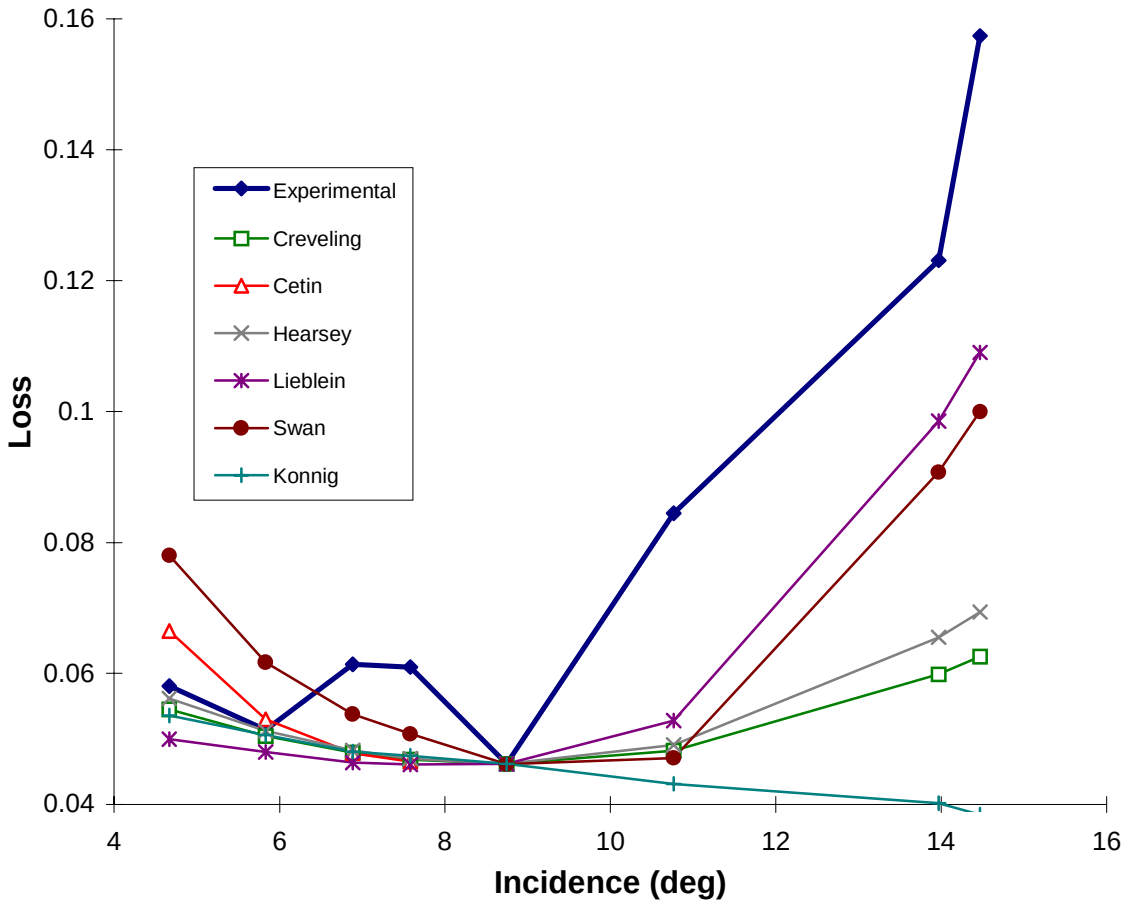

Figure 4.7 Rotor 1-B Loss Curves at 50% Speed

Unlike the 90% speed, the experimental data in Figure 4.7 for the 50% speed appears less well-behaved in the choked regime. This is likely due to the fact that the rotor is operating at a speed far from its design point.

None of the correlations gave acceptable errors on the stall side. The Lieblein correlation presented the minimal error in this regime with an RMS error of 0.0363. The experimentally measured data on the choke side of the 50% speed line was represented

well by all correlations tested in this regime. The best was Hearsey, with an RMS error of 0.0097. All six correlations displayed RMS errors of less than 0.0129.

Off-minimum-loss deviation angles were evaluated for Rotor 1-B. Figures 4.8, 4.9, 4.10, and 4.11 contain the graphs of deviation angle versus incidence for the experimental and the correlated predicted values for the 100%, 90%, 70%, and 50% corrected speeds, respectively. As mentioned in the data reduction section, the predicted deviation angle curves were translated onto the experimentally found deviation angle at the minimum-loss incidence. A summary of the results is found in Table 4.4.

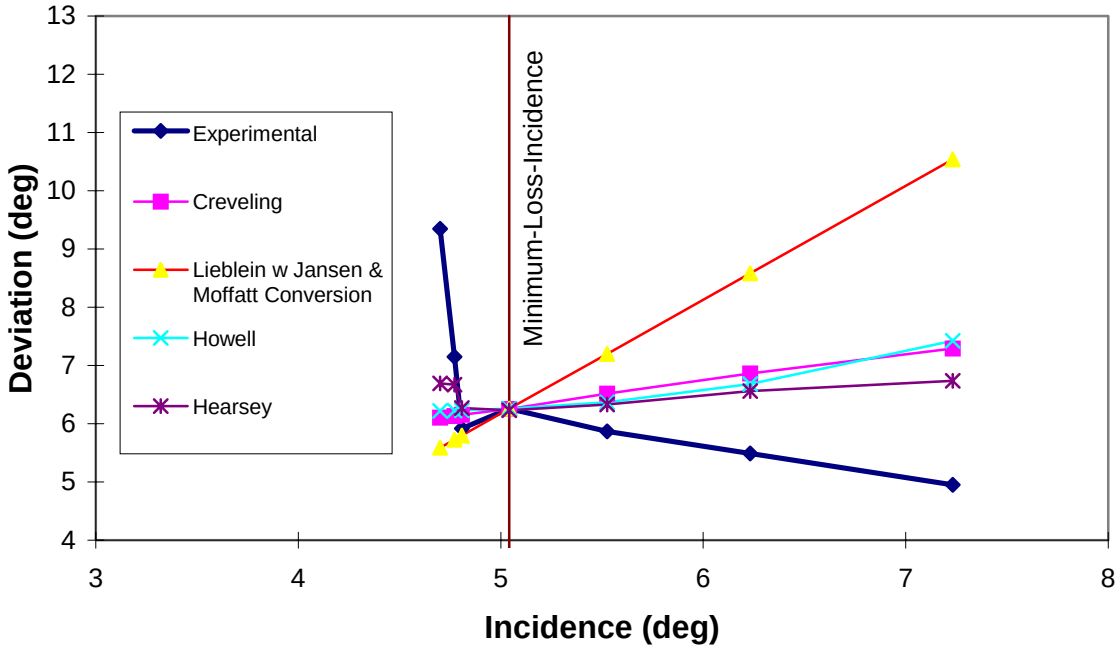

Figure 4.8 Rotor 1-B Deviation Angle Curves at 100% Speed

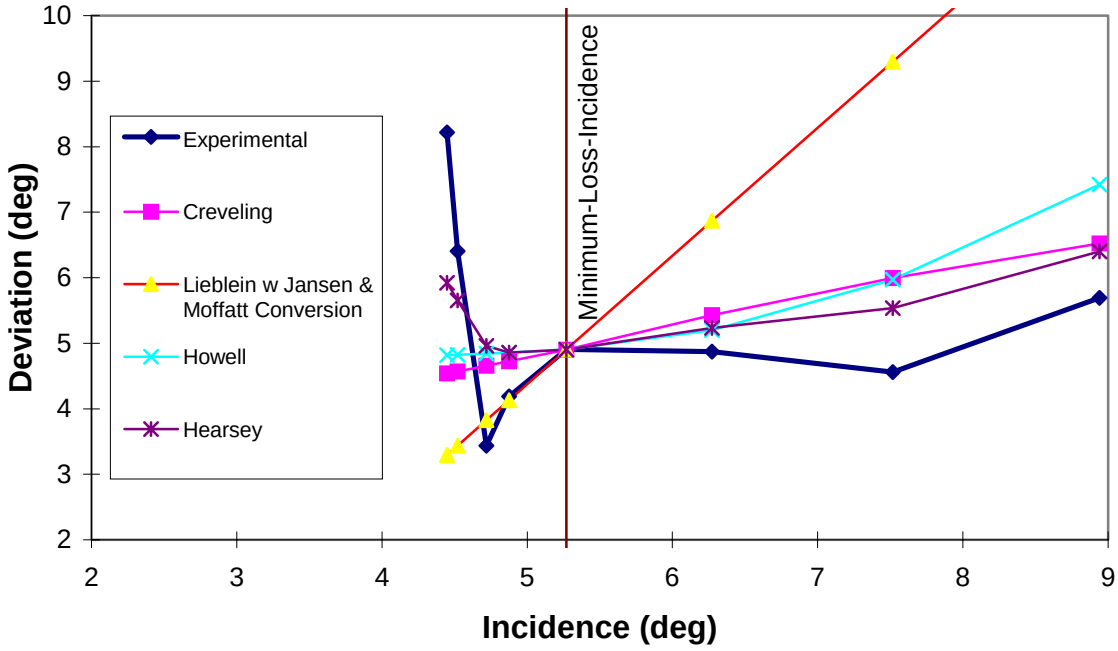

Figure 4.9 Rotor 1-B Deviation Angle Curves at 90% Speed

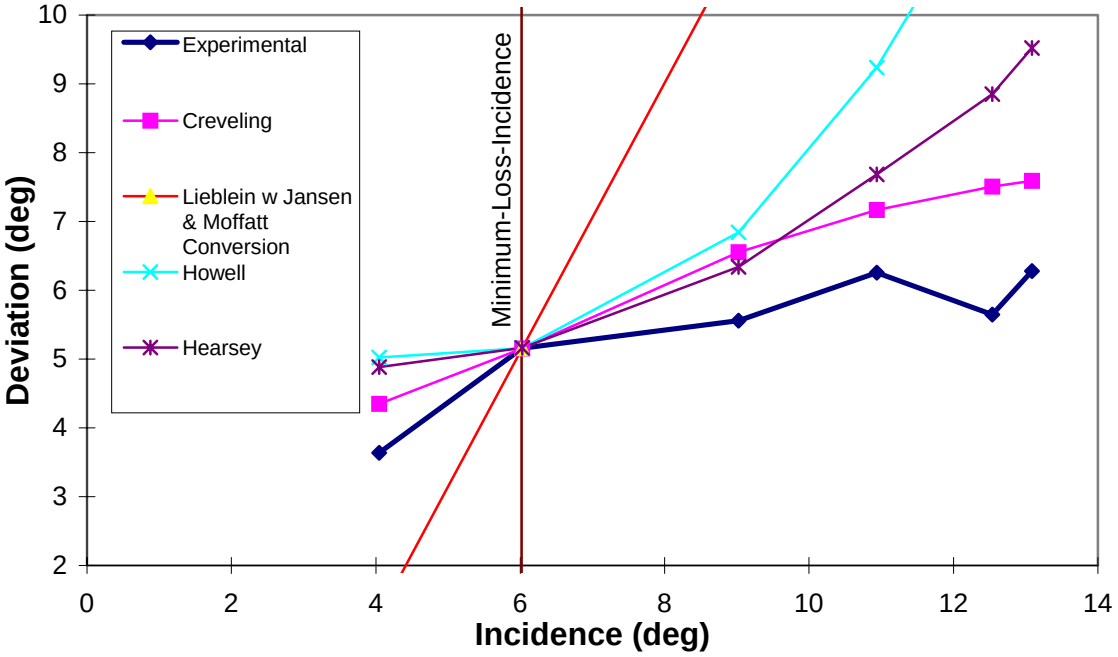

Figure 4.10 Rotor 1-B Deviation Angle Curves at 70% Speed

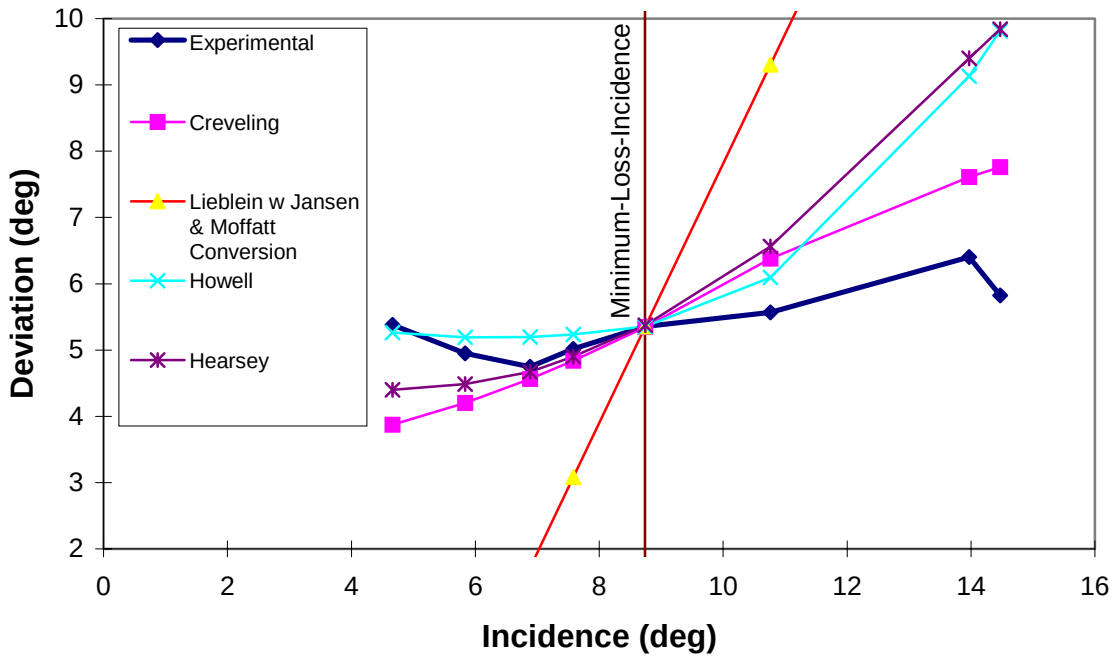

Figure 4.11 Rotor 1-B Deviation Angle Curves at 50% Speed

Table 4.4 summarizes the results of the off-minimum-loss deviation angle evaluation for Rotor 1-B. The evaluation contains the RMS errors between the experimental data and the correlations.

Table 4.4 Rotor 1-B RMS Error Analysis of Off-Minimum-Loss Deviation Angle

% Speed	Regime	Creveling (deg)	Lieblein w Jansen & Moffatt Conversion (deg)	Howell (deg)	Hearsey's Model (deg)
100	Stall	1.61	3.77	1.61	**1.23**
90	Stall	1.01	4.74	1.30	**0.73**
70	Stall	**1.32**	10.14	4.97	2.42
50	Stall	**1.40**	8.41	2.81	2.95
100	Choke	1.97	2.32	1.89	**1.57**
90	Choke	2.16	2.88	2.03	**1.47**
70	Choke	**0.51**	5.57	1.92	1.55
50	Choke	0.85	5.13	**0.28**	0.55

The Creveling, Hearsey model, and Howell correlations all performed fairly accurately over the entire region tested. The correlation that resulted in the minimum RMS error for each speed and regime is highlighted in bold in Table 4.4.

4.3 Evaluation of Models with NASA Stage 35

4.3.1 Rotor 35 Minimum-Loss Incidence, Deviation Angle, and Loss Prediction

Table 4.5 shows the minimum-loss predictions of NASA SP-36 and the Hearsey model, also known as CPAC.

Table 4.5 Rotor 35 Evaluation of Minimum-Loss Incidence Prediction

% Speeds	Experiment (deg)	NASA SP-36 (deg)	Hearsey (deg)
100	3.02	9.35	5.25
90	3.3	9.35	2.46
70	4.51	8.22	4.18
Mean Error		**5.37**	**1.13**

The Hearsey model showed a much better agreement with the experimentally measured data than did NASA SP-36, with a mean error of only 1.13°. The Hearsey model also predicted the minimum-loss incidence for the 70% and the 90% speeds to within 1°. For the 100% speed, the Hearsey model exhibited a greater error of 2°.

Table 4.6 shows the minimum-loss deviation angles for Rotor 35.

Table 4.6 Rotor 35 Evaluation of Minimum-Loss Deviation Angle Prediction

% Speed	Experimental (deg)	Hearsey (deg)	Carter f(B_2') (deg)	Modified by Cetin (deg)	Carter f(stagger) (deg)	Modified by Cetin (deg)
100	3.8	0.74	4.20	8.07	3.26	6.63
90	3.3	0.81	4.20	8.07	3.26	6.63
70	3.6	0.80	4.20	8.07	3.26	6.63
	Mean Error	**2.78**	**0.63**	**4.50**	**0.31**	**3.06**

The Carter models, one a function of blade metal angle and the other a function of blade stagger angle, displayed the least error when compared to the experimental results, with only 0.31° and 0.63° error in minimum-loss deviation angle predictions. When the Carter models were modified by Cetin, they predicted deviation angles that were far above experimental results. Conversely, the Hearsey model severely under-predicted the minimum-loss deviation angles.

The same methodology used to evaluate minimum-loss correlations for Rotor 1-B was used to evaluate minimum-loss correlations for Rotor 35. As Rotor 35 did not have a mid-span damper, the damper loss correlations were unnecessary. Therefore, the total predicted loss for Rotor 35 consisted of the sum of the blade profile and shock losses.

Table 4.7 contains the eight possible combinations of loss models used to obtain a total minimum-loss prediction.

Table 4.7 Rotor 35 Evaluation of Minimum-Loss Prediction

Experimental Total Minimum Loss	Koch + Koch	Koch + Miller	Lieblein + Koch	Lieblein + Miller	Swan + Koch	Swan + Miller	Hearsey + Koch	Hearsey + Miller
0.1230	0.117	0.114	0.126	0.122	0.181	0.177	0.140	0.137
0.093	0.059	0.062	0.065	0.067	0.087	0.090	0.086	0.089
0.044	0.016	0.016	0.018	0.018	0.021	0.021	0.044	0.044
MEAN ERROR	**0.023**	**0.023**	**0.019**	**0.017**	**0.029**	**0.027**	**0.008**	**0.006**

The titles for the predictions contain the names of the blade profile loss model + shock loss model. The second, third, and fourth rows of the table contain the total minimum-loss results from Rotor 35's 100%, 90%, and 70% corrected speed lines, respectively. It should be stated that the 100% and 90% corrected speed lines contained supersonic relative inlet Mach numbers, and the 70% corrected speed line contained subsonic relative inlet Mach numbers. At subsonic relative inlet Mach numbers, no shock loss model was included in the predictions. Over the entire range of corrected speeds, the combination of Hearsey profile and the Miller-Hartmann-Lewis shock loss models, and the combination of Hearsey profile and the Koch-Smith shock loss models gave predictions most comparable to Rotor 35 experimental data with mean loss errors of only 0.006 and 0.008, respectively. The next best combination was Leiblein profile and Miller-Hartmann-Lewis shock loss models, which gave a mean loss error of 0.017. Unlike for Rotor 1-B, the Koch-Smith combination of profile and shock was not very accurate, with a mean loss error of 0.023.

4.3.2 Rotor 35 Off-Minimum-Loss and Deviation Angle Prediction

Figure 4.12 shows predicted and experimental loss curves for Rotor 35 at 100% speed. The range of relative inlet Mach numbers for this speed was 1.31 to 1.40. Only the stall regime is shown in Figures 4.8, 4.9, and 4.10 due to the lack of experimental data for Rotor 35 in the choked regime.

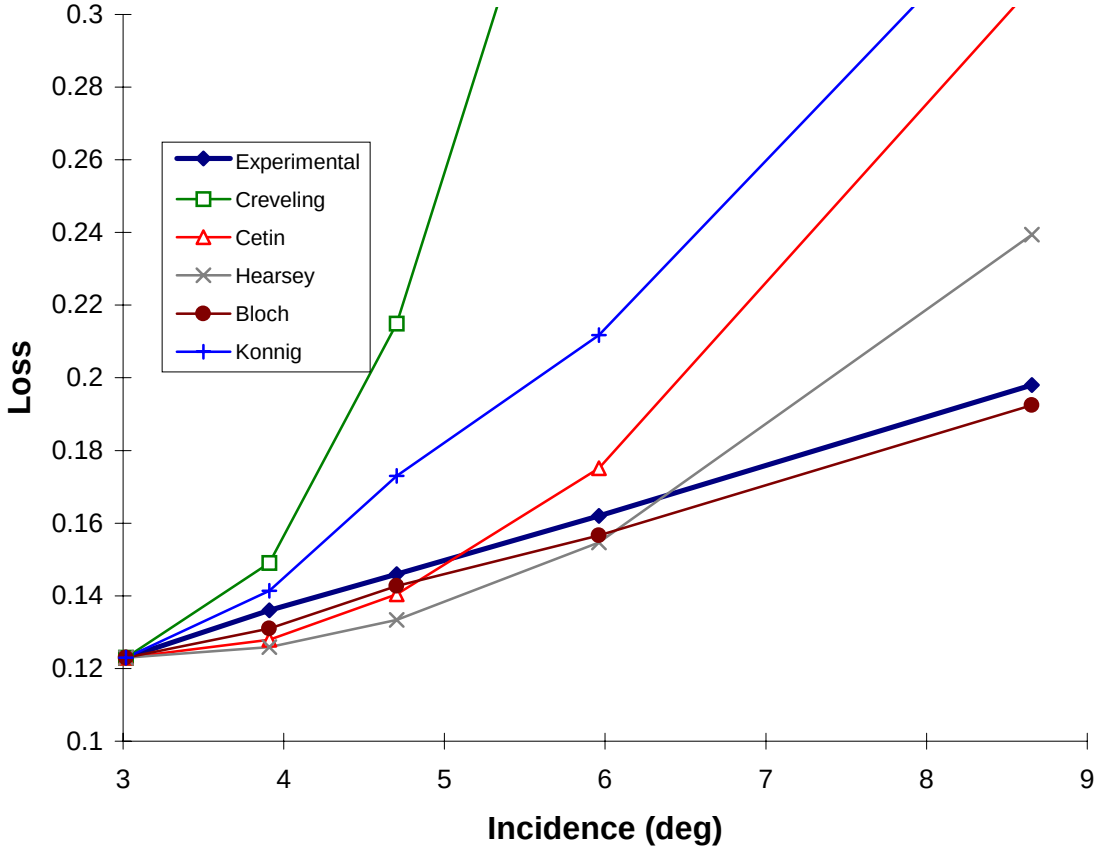

Figure 4.12 Rotor 35 Loss Curves at 100% Speed

In Figure 4.12, the experimental curve appears to be almost linear. The Bloch model also has linear trending of similar slope to the experiment, resulting in excellent agreement to the experiment with an RMS error of 0.0049. The next best correlation was the Hearsey model, with an RMS error of 0.023. The remaining correlations performed poorly when compared with experimental data.

Figure 4.13 shows predicted and experimental loss curves for Rotor 35 at 90% speed, and also shows a linear trend in experimental data. The range of relative inlet Mach numbers for this speed was 1.16 to 1.25.

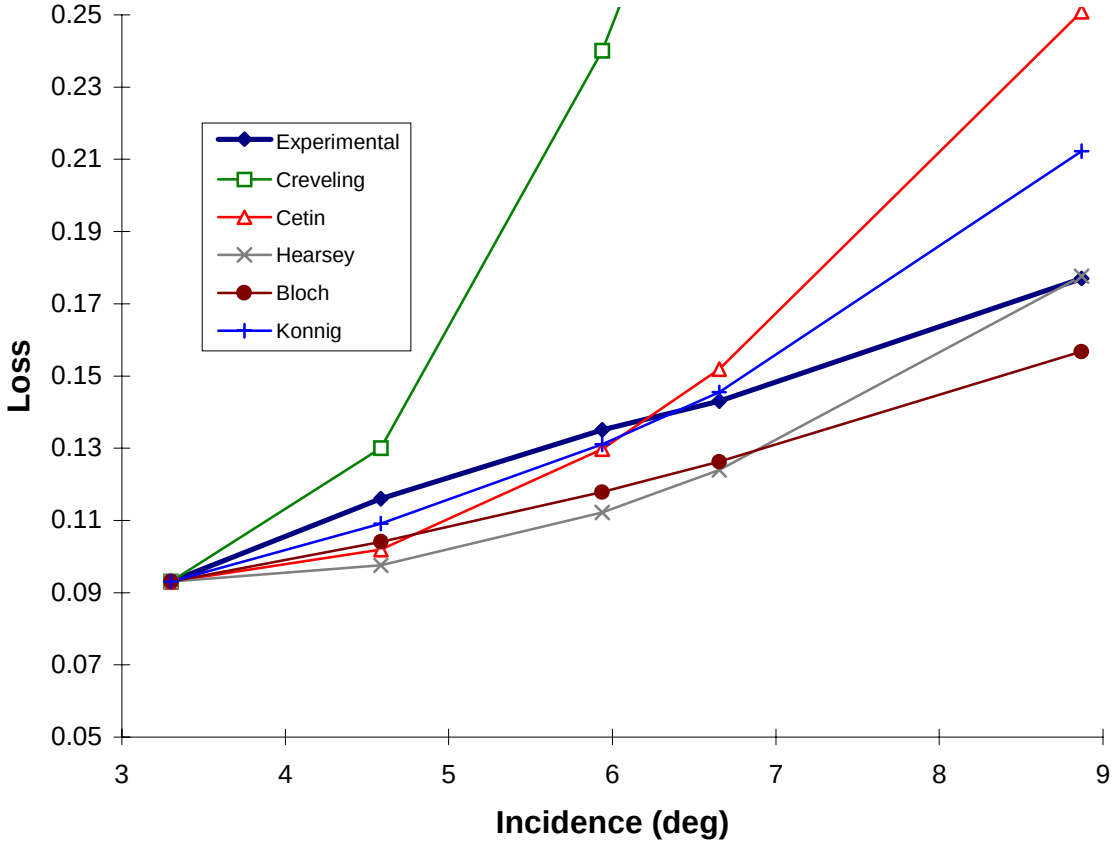

Figure 4.13 Rotor 35 Loss Curves at 90% Speed

In Figure 4.13, the slope of the Bloch prediction is less similar to the experimental curve than it was in Figure 4.12 for Rotor 35 at 100% speed. However, it still provides the best prediction, with an RMS error of 0.017. The Hearsey model had an RMS error of 0.0175 when compared with experimental data.

Figure 4.14 shows predicted and experimental loss curves for Rotor 35 at 70% speed. The range of relative inlet Mach numbers for this speed was 0.88 to 0.94.

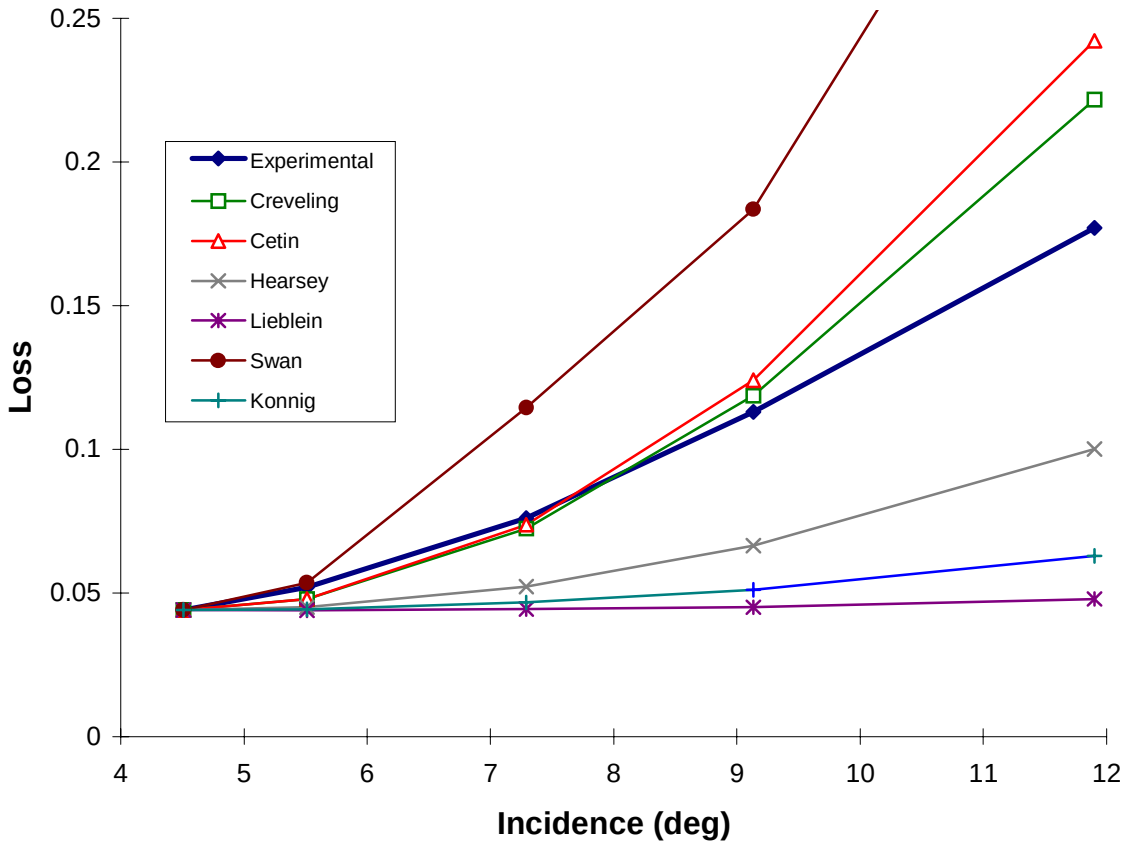

Figure 4.14 Rotor 35 Loss Curves at 70% Speed

None of the models in Figure 4.14 compared well with the experimental data for this speed. The Creveling correlation predicted the curve best, with an RMS error of 0.023. This is the second case in which the Creveling correlation showed any promise as compared to the other correlations, the first case being Rotor 1-B at 50% speed in the choked regime. The Cetin correlation had the next best result, with an RMS error of 0.033.

Off-minimum-loss deviation angles were evaluated for Rotor 35. Figures 4.15, 4.16, and 4.17 contain the graphs of deviation angle versus incidence for the experimental and the correlated predicted values for the 100%, 90%, and 70% corrected speeds, respectively. An evaluation of the off-minimum-loss deviation angle predictions can be found in Table 4.8 and the subsequent discussion.

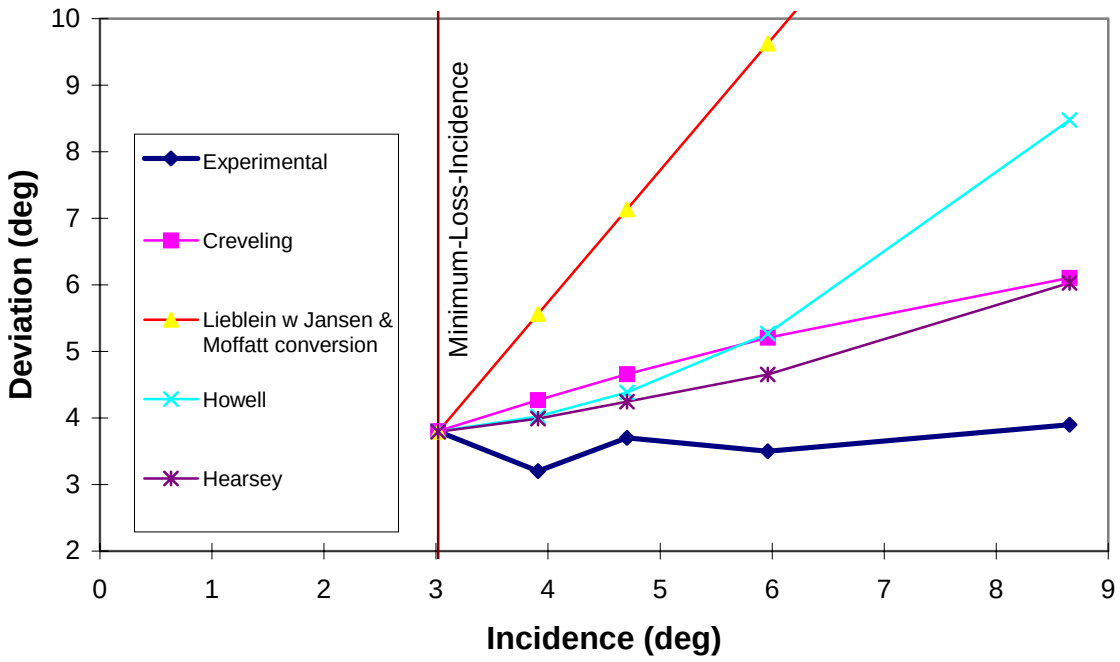

Figure 4.15 Rotor 35 Deviation Angle Curves at 100% Speed

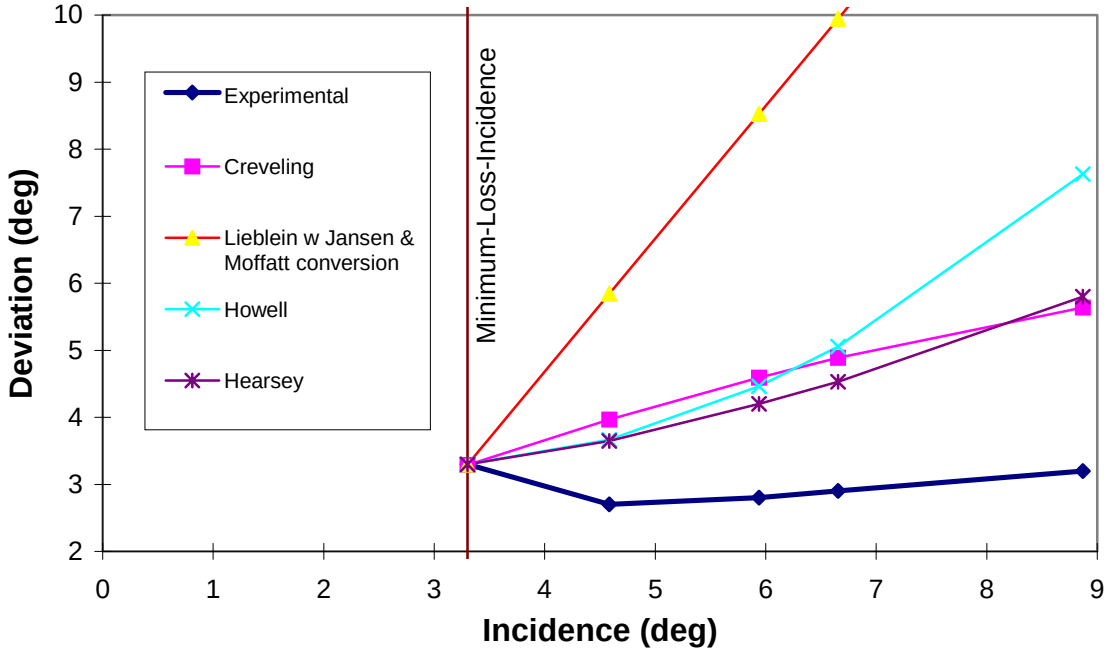

Figure 4.16 Rotor 35 Deviation Angle Curves at 90% Speed

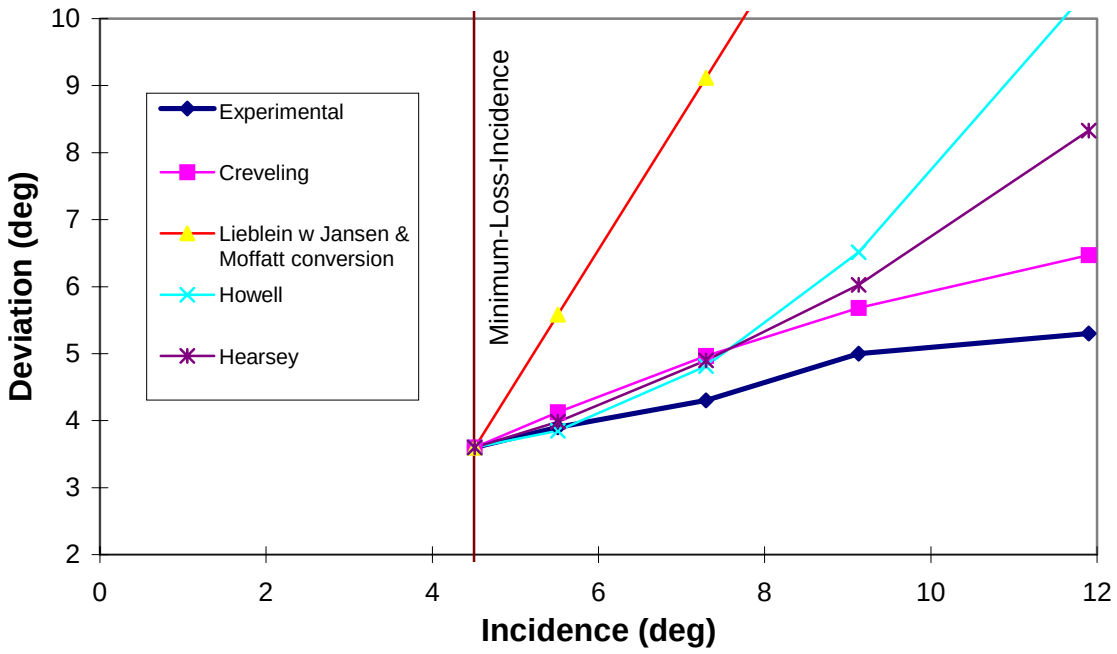

Figure 4.17 Rotor 35 Deviation Angle Curves at 70% Speed

Table 4.8 shows an RMS error analysis for off-minimum-loss deviation angles for Rotor 35.

Table 4.8 Rotor 35 RMS Error Analysis of Off-Minimum-Loss Deviation Angle

% Rotor Speed	Creveling (deg)	Lieblein w Jansen & Moffatt conversion (deg)	Howell (deg)	Hearsey Model (deg)
100	1.57	6.65	2.51	1.30
90	2.08	18.51	7.28	0.53
70	2.67	17.97	9.81	1.42

The Hearsey model showed the best qualitative results among correlations tested, with a maximum RMS error of less than 1.5°. The Creveling correlations also performed reasonably well, giving a mean error of 2.1° for the three speeds tested. Both the Howell

and Lieblein/Jansen/Moffatt correlations performed poorly, giving extremely high RMS errors.

4.3.3 Stator 35 Minimum-Loss Incidence, Deviation Angle, and Loss Prediction

Table 4.9 shows Stator 35 minimum-loss incidence prediction and experimental results. The speeds referred to in tables regarding Stator 35 are those for Rotor 35, which is rotating upstream of Stator 35.

Table 4.9 Stator 35 Evaluation of Minimum-Loss Incidence Prediction

% Speeds	Experiment (deg)	NASA SP-36 (deg)	Hearsey (deg)
100	-2	2.78	4.30
90	-3.4	1.94	3.79
70	-8.7	-0.64	2.21
Mean Error		**6.06**	**8.13**

Unlike for Rotor 1-B and Rotor 35, NASA SP-36 predicted the minimum-loss incidence better than the Hearsey model. However, the mean error for all speeds for both predictions was very poor at 6.06° and 8.13°, respectively.

Table 4.10 shows Stator 35 minimum-loss deviation angle prediction and experimental results.

Table 4.10 Stator 35 Evaluation of Minimum-Loss Deviation Angle Prediction

% Speed	Experimental (deg)	Hearsey (deg)	Carter $f(B_2')$ (deg)	Modified by Cetin (deg)	Carter f(stagger) (deg)	Modified by Cetin (deg)
100	7.8	5.87	6.97	10.28	6.81	10.24
90	7.5	5.94	6.97	10.28	6.81	10.24
70	6.2	6.01	6.97	10.28	6.81	10.24
	Mean Error	**1.23**	**0.71**	**3.12**	**0.76**	**3.07**

Again, both Carter models performed well as they did in Rotor 35, with mean errors of 0.71° and 0.76°. The Hearsey model also performed well, with mean errors of 1.23°. The Carter correlation modified by Cetin over-predicted the minimum-loss deviation angle by a mean of 3.12°.

As Stator 35 had no mid-span damper and the inlet relative Mach number was subsonic, the blade profile loss was assumed to equal the total loss. This facilitated evaluation of the minimum-loss correlations for Stator 35. Table 4.11 contains the four blade profile loss models used to obtain a total minimum-loss prediction.

Table 4.11 Stator 35 Evaluation of Minimum-Loss Prediction

Inlet Mach Number	Experimental Minimum Loss	Koch	Lieblein	Swan	Hearsey
0.7710	0.0400	0.0140	0.0154	0.0175	0.0371
0.729	0.026	0.0153	0.0157	0.0162	0.0371
0.581	0.029	0.0197	0.0171	0.0166	0.0371
MEAN ERROR		**0.0153**	**0.0156**	**0.0149**	**0.0074**

The Hearsey model predicted minimum-loss best with a mean error of only 0.0074. Koch and Smith, Lieblein, and Swan blade profile loss predictions all displayed a mean error of approximately 0.015.

4.3.4 Stator 35 Off-Minimum-Loss and Deviation Angle Prediction

Figure 4.18 shows the loss predicted by correlations and experiment for Stator 35 at 100% rotor speed. The range of Mach numbers at the inlet to the stator for this rotor speed was 0.75 to 0.77.

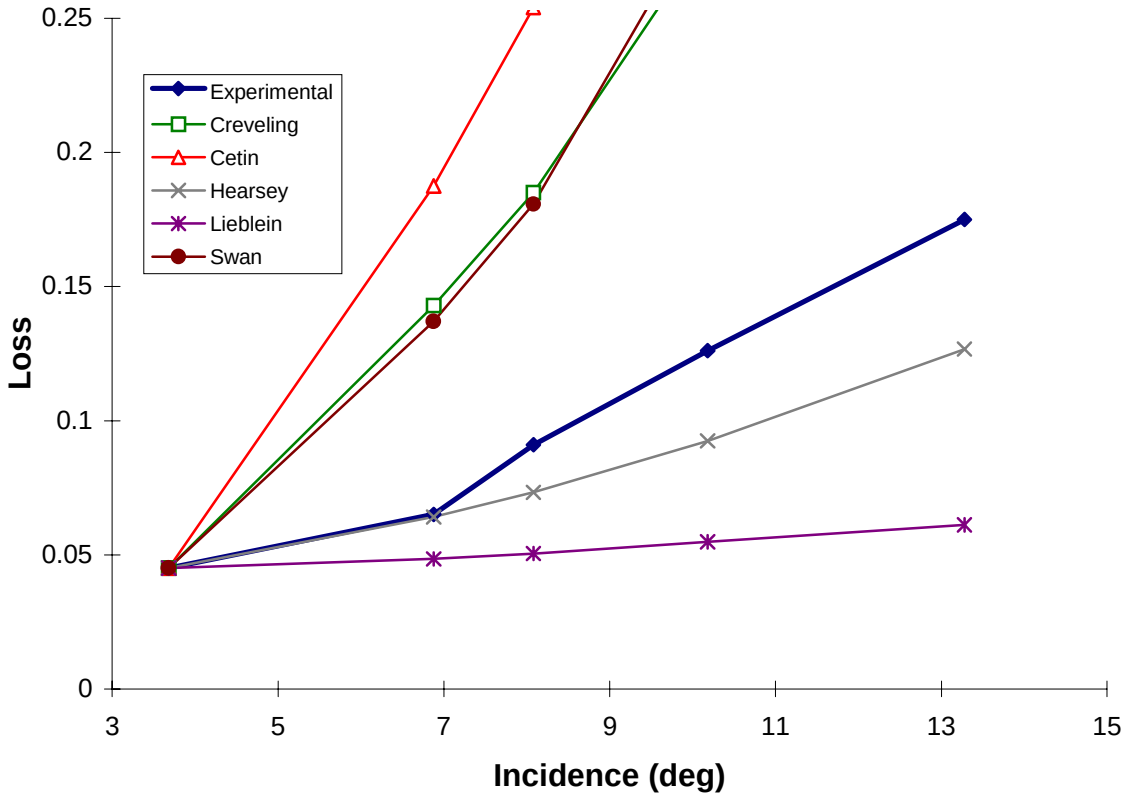

Figure 4.18 Stator 35 Loss Curves at 100 % Rotor Speed

Among the predictions in Figure 4.18, Hearsey and Lieblein performed best with RMS errors of 0.03 and 0.07, respectively. Although the accuracy of these predictions were unacceptable, the remainder of the correlations performed far worse, all with RMS errors of over 0.16. The Konnig correlation would not converge to an answer for any Stator 35 results.

Figure 4.19 shows the loss predicted by correlations and experiment for Stator 35 at 90% rotor speed. The range of Mach numbers at the inlet to the stator for this rotor speed was 0.69 to 0.73.

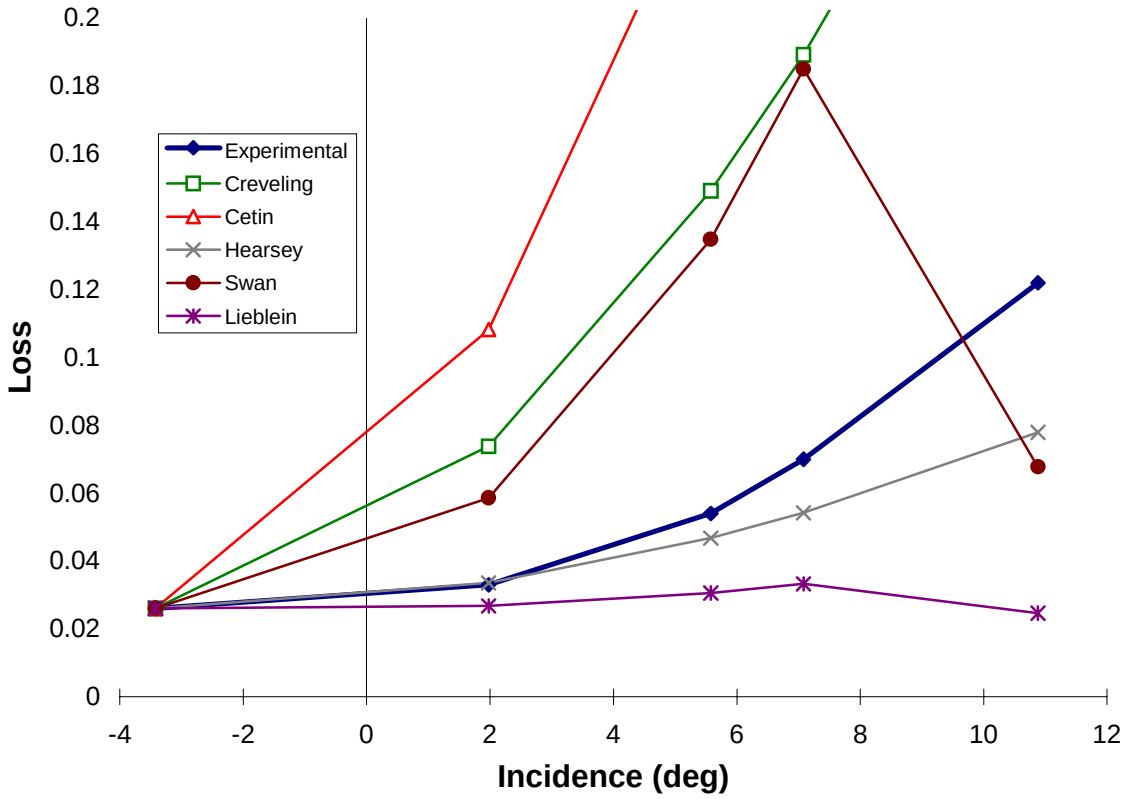

Figure 4.19 Stator 35 Loss Curves at 90% Rotor Speed

All correlations performed better than they did at 100% rotor speed, although their results were still unacceptably poor. The Hearsey model performed best, with an RMS error of 0.024.

Figure 4.20 shows the loss predicted by correlations and experiment for Stator 35 at 70% rotor speed. The range of Mach numbers at the inlet to the stator for this rotor speed is 0.52 to 0.60.

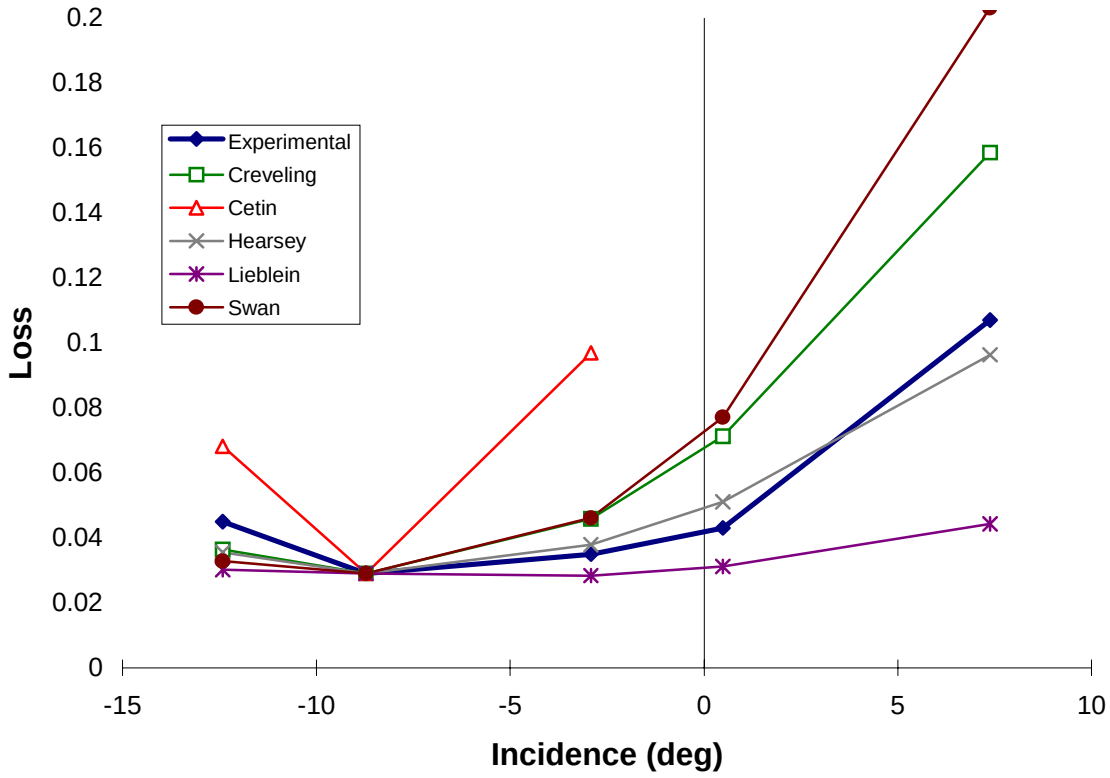

Figure 4.20 Stator 35 Loss Curves at 70% Rotor Speed

Again, every correlation in Figure 4.20 improved over previous results for Stator 35 at 100% and 90% rotor speeds. The Hearsey model once again performed best, with an RMS error of 0.0083. Note that the Hearsey model performed better than all other correlations for all tested Stator 35 rotor speeds, and it was the only model remotely close to experimental results for Stator 35 at 70% rotor speed.

Off-minimum-loss deviation angles were evaluated for Stator 35. Figures 4.21, 4.22, and 4.23 contain the graphs of deviation angle versus incidence for the experimental and the correlated predicted values for the 100%, 90%, and 70% corrected rotor speeds, respectively. An evaluation of the off-minimum-loss deviation angle predictions can be found in Table 4.12 and the subsequent discussion.

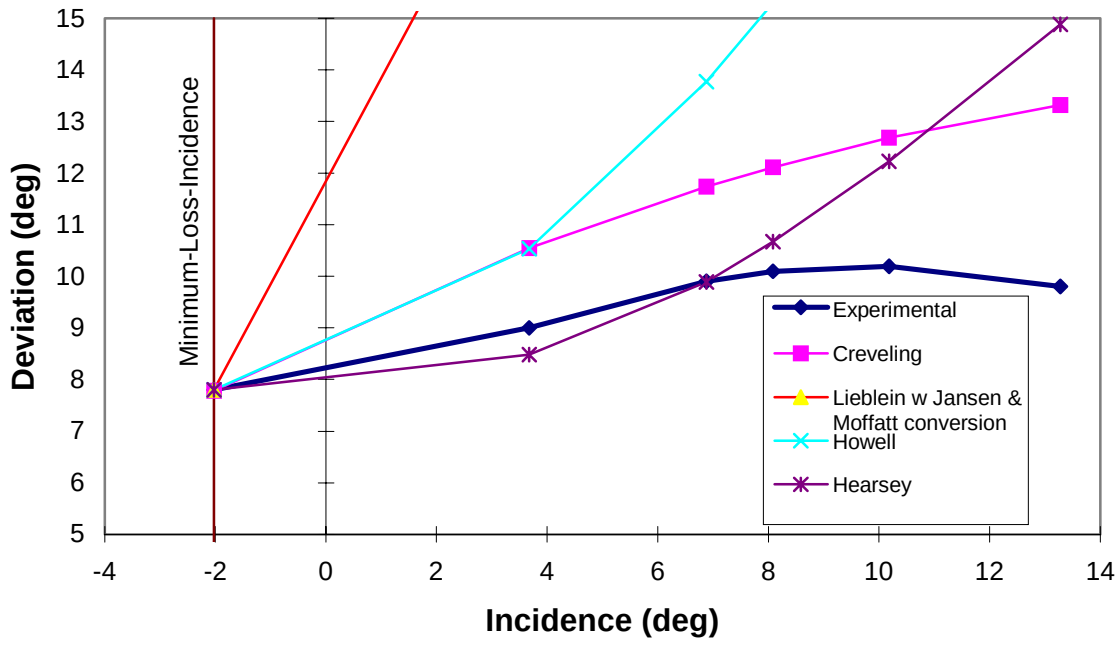

Figure 4.21 Stator 35 Deviation Angle Curves at 100% Rotor Speed

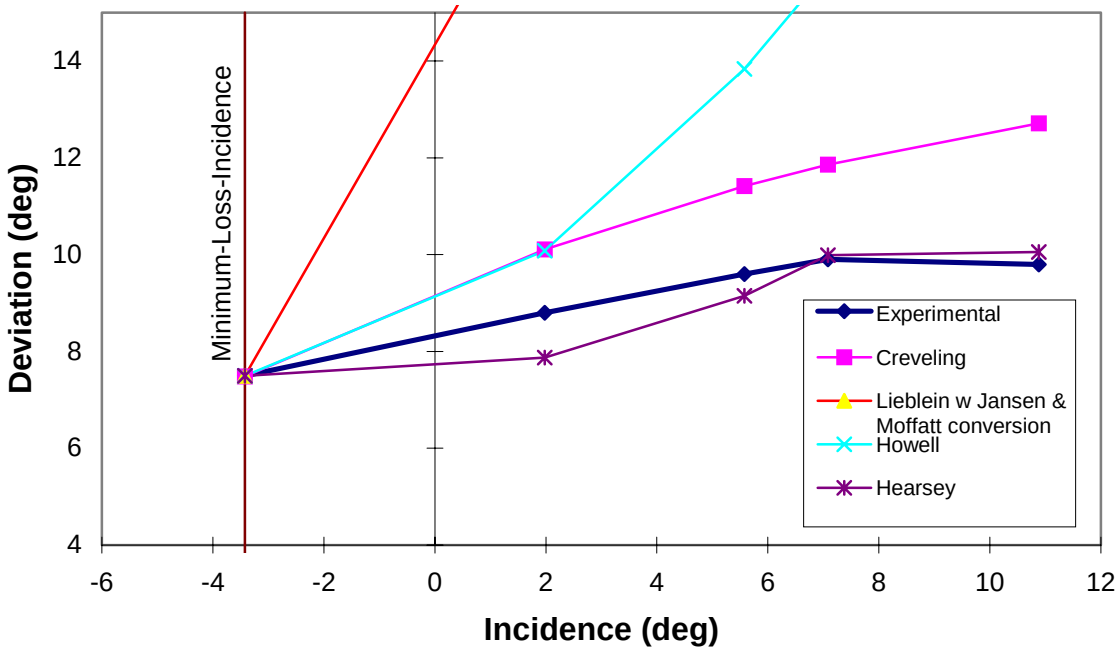

Figure 4.22 Stator 35 Deviation Angle Curves at 90% Rotor Speed

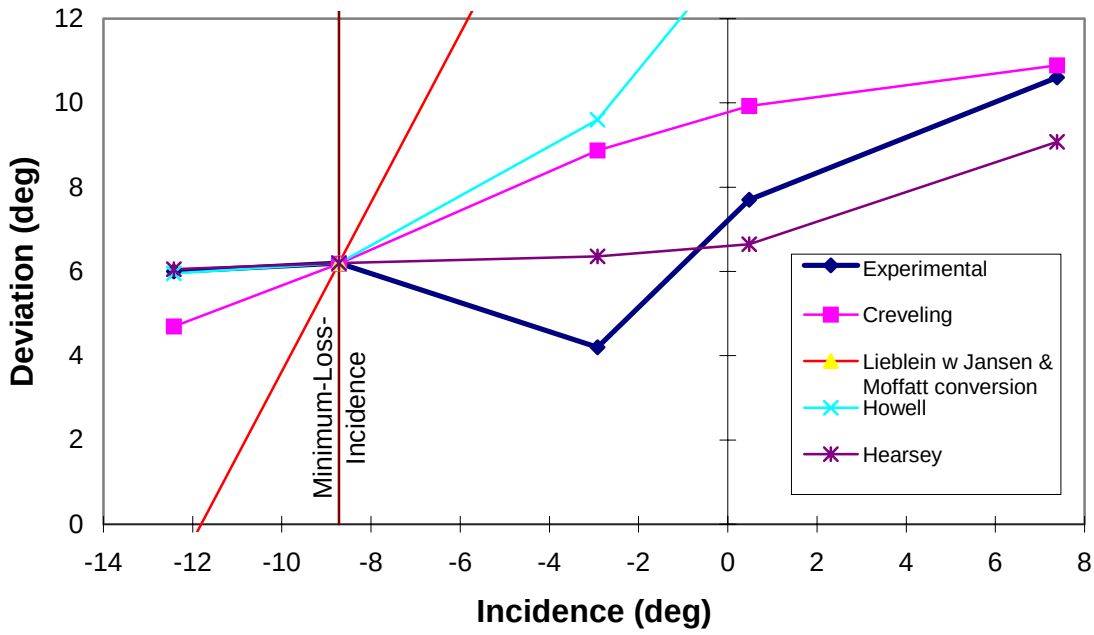

Figure 4.23 Stator 35 Deviation Angle Curves at 70% Rotor Speed

Table 4.12 shows RMS error of off-minimum-loss deviation angles for Stator 35.

Table 4.12 Stator 35 RMS Error Analysis of Off-Minimum-Loss Deviation Angle

% Rotor Speed	Creveling (deg)	Lieblein w Jansen & Moffatt conversion (deg)	Howell (deg)	Hearsey Model (deg)
100	**2.38**	19.76	7.88	2.47
90	2.08	18.51	7.28	**0.53**
70	2.67	17.97	9.81	**1.42**

Again, the Hearsey and Creveling correlation gave the best results for Stator 35. The RMS errors for the best prediction at each speed are highlighted in Table 4.12. Both Howell and Lieblein correlations gave extremely high RMS errors and it is recommended that they not be used to model this particular experiment.

Chapter 5.0 Conclusions and Recommendations for Future Work

The prediction of minimum-loss incidence is a key factor in calculating loss and deviation points for all correlations, as any error in this incidence will propagate itself through the remaining loss and deviation predictions. Therefore, it is critical that predictions of the minimum-loss incidence be highly accurate.

In the area of minimum-loss prediction there was no single method that could be considered universally applicable. The Koch and Smith model is considered the best design-loss point predictor for a transonic rotor (Cetin, 1987 and Konnig, Part I, 1996). While the author agrees that the Koch and Smith loss model is the most comprehensive and theoretically sound loss model reviewed, it performed poorly in the minimum-loss prediction for Stage 35 (see Tables 4.7 and 4.11).

A new method was created in order to qualitatively evaluate off-minimum-loss correlations. Translating the off-minimum-loss curves onto the experimental minimum-loss point effectively isolates the off-minimum-loss predictions and eliminates errors which may be included in minimum-loss predictions.

The Bloch shock loss model displayed promise as a good qualitative predictor for total loss in the stall regime for supersonic inlet relative Mach numbers (see Figures 4.4, 4.5, 4.12, and 4.13). This suggested that profile loss is relatively constant in the supersonic stall regime as claimed by Bloch and Schreiber. However, the Bloch model quantitatively over-predicted shock loss. This can be stated with confidence because at times the Bloch model gave shock losses greater than the total loss through the blade as measured in the experiments.

None of the correlations tested provided accurate predictions in the choke regime of Rotor 1-B for 90% and 100% speeds. More research, both experimental, analytical, and computational, must be done in order to improve understanding of the difference in

shock structures between 2-D transonic cascades and 3-D transonic rotors in the choke regime. Bloch (1996) suggested that the difference is a result of subsonic flow that exists in the casing boundary layer of the 3-D rotor that is not present in 2-D cascades. This subsonic region allows for downstream pressure information to influence the upstream flow conditions and shock structures. Downstream pressure information cannot travel fast enough upstream through the sonic or supersonic regions found in the 2-D cascades. This may explain why there exists a smooth transition from the started/unstarted regimes in the 3-D rotor and not in 2-D cascades.

Predicting accurate deviation angles is equally important as predicting accurate loss models in order to obtain accurate stage characteristics. The Hearsey and Creveling off-minimum-loss deviation angle prediction performed consistently better than all other correlations tested (see Tables 4.4, 4.8, and 4.12). However, in the current evaluation, the accuracy criteria chosen was commonly unmet.

The current evaluation is an assessment of the correlation accuracies based on the experimental data for Rotor 1-B and Stage 35. There were many differences in results between the two machines. This suggests that these correlations should be re-evaluated against experimental data from many other rotors and stators before a complete assessment of the accuracy and applicability of each correlation can be made. As with any investigation of predictions, the larger the experimental data base, the more confident the results.

The current investigation focused only on the meanline predictions. In order to build more accurate stage characteristics, one must be able to predict the entire spanwise flowfield. Therefore, the correlations must be evaluated over the entire span of the blade.

Chapter 6.0 References

Bloch, G.S., Copenhaver, W.W., O'Brien, W.F., "Development of an Off-Design Loss Model for Transonic Compressor Design," AGARD CP-571, Paper 16, 1995.

Bloch, G.S., "Flow Losses in Supersonic Compressor Cascades," Ph.D. Dissertation, Virginia Polytechnic Institute and State University, Blacksburg, VA, July 1996.

Cetin, M., Ucer, A.S., Hirsch, Ch., and Serovy, G.K., "Application of Modified Loss and Deviation Correlations to Transonic Axial Compressors" AGARD Report No. 745 November 1987.

Cohen, H., Rogers, G.F.C., Saravanamuttoo, H.I.H., Gas Turbine Theory. Longman Scientific and Technical, England. 1987. 3rd Edition.

Creveling, H.F., "Axial-Flow Compressor Computer Program for Calculating Off-Design Performance," NASA CR 72472, 1968.

Hale, A.A., "A Three-Dimensional Turbine Engine Analysis Compressor Code (TEACC) for Steady-State Inlet Distortion," Ph.D. Dissertation, Virginia Polytechnic Institute and State University, Blacksburg, VA, December 1996.

Hearsey, R.M., "HT0300-A Computer Program for the Design and Analysis of Axial Turbomachinery," Parts I-II, Cambridge, Massachusetts, March 1970.

Hill, P.G., Peterson, C.R., Mechanics and Thermodynamics of Propulsion. Addison-Wesley, Reading, Massachusetts: 1967.

Howell, A.R., “Development of British Gas Turbine Unit, Lecture: Fluid Dynamics of Axial Compressors,” ASME Reprint 1947.

Jansen, W., Moffatt, W.C., “The Off-Design Analysis of Axial-Flow Compressors,” ASME Journal of Engineering for Power, Vol. 89, 1967, pp. 453-462.

Koch, C.C., Smith, L.H., “Loss Sources and Magnitudes in Axial-Flow Compressors,” ASME Journal of Engineering for Power, Vol. 98, 1976, pp. 411-424.

Konnig, W.M., Hennecke, D.K., Fottner, L., “Improved Blade Profile Loss and Deviation Angle Models for Advanced Transonic Compressor Bladings: Part I - A Model for Subsonic Flow,” ASME Journal of Turbomachinery, Vol. 118, 1996, pp. 73-80.

Konnig, W.M., Hennecke, D.K., Fottner, L., “Improved Blade Profile Loss and Deviation Angle Models for Advanced Transonic Compressor Bladings: Part II - A Model for Supersonic Flow,” ASME Journal of Turbomachinery, Vol. 118, 1996, pp. 81-87.

Lieblein, S., “Analysis of Experimental Low-Speed Loss and Stall Characteristics of Two-Dimensional Compressor Blade Cascades,” NASA RM E 57A28, 1957.

Lieblein, S., “Viscous Flow in Two-dimensional Cascades,” NASA SP-36, Chapter 5, 1965.

Leiblein, S., “Experimental Flow in Two-dimensional Cascades,” NASA SP-36, Chapter 6, 1965.

Leiblein, S., “Blade Element Flow in Annular Cascades,” NASA SP-36, Chapter 7, 1965.

Miller, G.R., Lewis, G.W., Hartmann, M.J., “Shock Losses in Transonic Compressor Blade Rows,” ASME Journal of Engineering for Power, Vol. 83, 1961, pp. 235-242.

Moses, H.L., “Fluid Machinery Design with Turbomachine Applications,” ME 4414 Fluid Machinery Design Course Notebook, Virginia Polytechnic Institute and State University, 1994.

Reid, L., Moore, R.D., “Performance of Single-Stage Axial-Flow Transonic Compressor with Rotor and Stator Aspect Ratios of 1.19 and 1.26, and with design Pressure Ratio of 1.82” NASA Technical Paper 1338 November 1978.

Schreiber, H.A., Starken, H., “Experimental Cascade Analysis of a Transonic Compressor Rotor Blade Section”, ASME Journal of Engineering for Gas Turbines and Power, Vol. 106, No. 2, April 1984.

Serovy, G.K.,”Performance Prediction for Axial-Flow Compressor and Turbine Blading,” AGARD Lecture Series 167, May 1989.

Seyler, D.R. Gostelow, J.P., “Single Stage Experimental Evaluation of High Mach Number Compressor Rotor Blading” NASA Lewis Research Center September 22, 1967.

Stewart, W.L., “Analysis of Two-Dimensional Compressible Flow Loss Characteristics Downstream of Turbomachinery Blade Rows in Terms of Basic Boundary Layer Characteristics,” NACA TN 3515, 1955.

Swan, W.C., “A Practical Method of Predicting Transonic Compressor Performance,” ASME Journal of Engineering for Power, Vol. 83, 1961, pp. 322-330.

Chapter 7.0 APPENDIX A NASA Rotor 1-B

NASA Rotor 1-B was a high performance transonic rotor similar to those found in modern high-speed aircraft (Seyler, 1967). It had 44 blades, a tip radius of 18.25", and a hub radius of 9.125". Rotor 1-B was designed with double-circular arc (DCA) blades for the bottom 60% span and multiple circular arc (MCA) over the top 40% span. For structural purposes, Rotor 1-B required a mid-span damper. At the 100% corrected speed line, Rotor 1-B produced a corrected mass flow rate of 219.2 lb./sec, an adiabatic efficiency of 89.5%, and a total pressure ratio of 1.63.

Table A1 shows Rotor 1-B blade geometry information at the meanline. Tables A2 through A5 contain Rotor 1-B experimental flow information at the meanline.

Table A1 Rotor 1-B Geometry at Meanline

Tip Radius	1.52 ft
Hub Radius	0.84 ft
Inlet Radius of Meanline	1.16 ft
Exit Radius of Meanline	1.17 ft
Chord Length (c)	0.24 ft
LER	0.00026 ft
t_{max}/c	.0685
Solidity (σ)	1.97
a/c	0.5
Inlet blade metal angle (β_1')	52.6 °
Exit blade metal angle (β_2')	43.8 °

Table A2 Rotor 1-B Meanline Flow information at 100% Speed

M_{1rel}	Incidence angle (β_i-β_i')	MVDR	Loss ϖ	Deviation angle δ	Rotor speed Ω
1.142	7.232	1.050	0.1109	4.95	921
1.161	6.232	1.039	0.1133	5.49	924
1.170	5.525	1.048	0.094	5.87	922
1.177	5.042	1.051	0.0971	6.26	921
1.181	4.808	1.045	0.1356	5.92	921
1.181	4.772	1.004	0.1828	7.15	921
1.183	4.700	1.001	0.1983	9.35	921

Table A3 Rotor 1-B Meanline Flow information at 90% Speed

M_{1rel}	Incidence angle (β_i-β_i')	MVDR	Loss ϖ	Deviation angle δ	Rotor speed Ω
1.001	8.941	1.048	0.104	5.69	828
1.022	7.516	1.073	0.069	4.56	831
1.035	6.273	1.066	0.0622	4.87	829
1.045	5.269	1.080	0.0443	4.91	827
1.055	4.875	1.079	0.0758	4.19	830
1.056	4.720	1.067	0.1243	3.43	829
1.059	4.520	0.997	0.1776	6.41	829
1.059	4.448	0.969	0.1952	8.22	828

Table A4 Rotor 1-B Meanline Flow information at 70% Speed

M_{1rel}	Incidence angle (β_i-β_i')	MVDR	Loss ϖ	Deviation angle δ	Rotor speed Ω
0.741	13.088	1.021	0.1617	6.28	644
0.744	12.539	1.040	0.1713	5.65	644
0.756	10.937	1.034	0.1283	6.26	644
0.772	9.023	1.054	0.0884	5.56	645
0.797	6.026	1.063	0.0494	5.16	644
0.815	4.047	1.067	0.092	3.64	642

Table A5 Rotor 1-B Meanline Flow information at 50% Speed

M_{1rel}	Incidence angle (β_i-β_i')	MVDR	Loss ϖ	Deviation angle δ	Rotor speed Ω
0.521	14.470	1.053	0.1574	5.82	460
0.523	13.968	1.047	0.1231	6.41	460
0.538	10.764	1.065	0.0845	5.57	460
0.548	8.743	1.068	0.0462	5.36	460
0.555	7.581	1.065	0.061	5.02	460
0.559	6.884	1.065	0.0614	4.75	460
0.565	5.834	1.058	0.0514	4.95	460
0.573	4.665	1.050	0.0581	5.38	460

Chapter 8.0 APPENDIX B NASA Stage 35

NASA Stage 35 consisted of a transonic low-aspect ratio rotor with 36 blades and a stator containing 46 blades (Reid, 1978). At the design speed, the rotor and the stage reached peak adiabatic efficiencies of 87.2% and 84.5% at pressure ratios of 1.875 and 1.842, respectively. No mid-span damper was present on the rotor.

Tables B1 and B5 provide the blade geometry at the meanline for the rotor and the stator. Tables B2 through B4 contain experimental flow information for the rotor at the meanline at given speeds. Tables B6 through B8 contain experimental flow information for the stator at the meanline for the corresponding Rotor 35 speeds. The accuracy of the experimental data is reviewed in Table B9.

Table B1 Rotor 35 Geometry at Meanline

Tip Radius	.833 ft
Hub Radius	0.5833 ft
Inlet Radius of Meanline	.7125 ft
Exit Radius of Meanline	.7088 ft
Chord Length (c)	0.1825 ft
LER	0.000617 ft
t_{max}/c	.056
Solidity (σ)	1.47
a/c	0.6
Inlet blade metal angle (β_1')	56.16°
Exit blade metal angle (β_2')	44.26°

Table B2 Rotor 35 Meanline Flow information at 100% Speed

M_{1rel}	Incidence angle (β_i-β_i')	MVDR	Loss ϖ	Deviation angle δ	Rotor Speed Ω
1.31	8.66	1.31	0.198	3.9	1803
1.35	5.96	1.28	0.162	3.5	1803
1.38	4.70	1.27	0.146	3.7	1803
1.38	3.91	1.27	0.136	3.2	1791
1.40	3.02	1.27	0.123	3.8	1792

Table B3 Rotor 35 Meanline Flow information at 90% Speed

M_{1rel}	Incidence angle (β_i-β_i')	MVDR	Loss ϖ	Deviation angle δ	Rotor Speed Ω
1.17	8.87	1.28	0.177	3.2	1619
1.20	6.65	1.27	0.143	2.9	1620
1.21	5.94	1.26	0.135	2.8	1620
1.23	4.58	1.27	0.116	2.7	1620
1.25	3.30	1.27	0.093	3.3	1619

Table B4 Rotor 35 Meanline Flow information at 70% Speed

M_{1rel}	Incidence angle (β_i-β_i')	MVDR	Loss ϖ	Deviation angle δ	Rotor Speed Ω
0.88	11.90	1.30	0.177	5.3	1258
0.90	9.13	1.28	0.113	5	1262
0.92	7.29	1.27	0.076	4.3	1264
0.94	5.51	1.27	0.052	3.9	1265
0.94	4.51	1.27	0.044	3.6	1261

Table B5 Stator 35 Geometry at Meanline

Tip Radius	.7933 ft
Hub Radius	0.6167 ft
Inlet Radius of Meanline	.708 ft
Exit Radius of Meanline	.710 ft
Chord Length (c)	0.1325 ft
LER	0.0004 ft
t_{max}/c	.0575
solidity (σ)	1.37
a/c	0.5
Inlet blade metal angle (β_1')	35.7°
Exit blade metal angle (β_2')	3.11°

Table B6 Stator 35 Meanline Flow information at 100% Rotor Speed

M_{1rel}	Incidence angle (β_i-β_i')	MVDR	Loss ϖ	Deviation angle δ
0.747	13.3	1.1396	0.175	9.8
0.755	10.2	1.1188	0.126	10.2
0.755	8.1	1.1207	0.091	10.1
0.761	6.9	1.1253	0.065	9.9
0.763	3.7	1.1208	0.045	9
0.771	-2.0	1.1093	0.04	7.8

Table B7 Stator 35 Meanline Flow information at 90% Rotor Speed

M_{1rel}	Incidence angle (β_i-β_i')	MVDR	Loss ϖ	Deviation angle δ
0.688	10.9	1.3717	0.122	9.8
0.698	7.1	1.1034	0.07	9.9
0.702	5.6	1.1084	0.054	9.6
0.714	2.0	1.1125	0.033	8.8
0.729	-3.4	1.1135	0.026	7.5

Table B8 Stator 35 Meanline Flow information at 70% Rotor Speed

M_{1rel}	Incidence angle $(\beta_i-\beta_i')$	MVDR	Loss ϖ	Deviation angle δ
0.524	7.4	1.0823	0.107	10.6
0.537	0.5	1.0811	0.043	7.7
0.554	-2.9	1.0974	0.035	4.2
0.581	-8.7	1.1068	0.029	6.2
0.604	-12.4	1.1211	0.045	6

The estimated error of the data in Tables B2 through B8 is based on the accuracy of the recorder and instrumentation and is listed in Table B9.

Table B9 Stage 35 Experimental Error

Mass flow kg/sec	+/- 0.3
Rotational Speed, rpm	+/- 30
Flow angle, deg	+/- 1.0
Temperature, K	+/- 0.6
Total pressure @ rotor inlet, N/cm^2	+/- 0.01
Static pressure @ rotor inlet, N/cm^2	+/- 0.03
Total pressure @ stator exit, N/cm^2	+/- 0.17
Static pressure @ stator exit, N/cm^2	+/- 0.10

Chapter 9.0 APPENDIX C AVDR - MVDR Relationships

Background

The Axial Velocity Density Ratio (**AVDR**) is widely used to measure the degree to which the flow streamtubes in a 2-D cascade are contracted (Schreiber, 1984). The axial component of velocity for subsonic flow in an experimental cascade will increase due to boundary layer effects, consequently changing the **AVDR**.

The value of the **AVDR** is normally quoted when listing results from 2-D cascades. When applying these results to the prediction of the performance of 3-D annular cascades, the **AVDR** must be altered so as to apply to the 3-D annular flow. In this investigation, a new parameter, the Meridional Velocity Density Ratio (**MVDR**), was developed to account for boundary layer effects in 3-D annular cascades. The following development relates the definition of the **MVDR** to the **AVDR**.

Linear Cascade Theory

The **AVDR** is a useful parameter when dealing with cascade flow. The ratio of areas perpendicular to the relative flow entering and exiting the blade row can be calculated directly if the **AVDR** and the relative flow angles are known. This ratio is necessary when computing the relative mass flow functions, which is one method used to cross the blade passage. Equation (C1) represents the definition of **AVDR**

$$\textbf{AVDR} = (\rho_2 V_{x2}) / (\rho_1 V_{x1}) \qquad \textbf{(C1)}$$

In Equation C1, ρ is the density, V_x the absolute axial velocity, and the subscripts (1) and (2) imply the inlet and exit of the blade rows, respectively. Because the blade velocity is perpendicular to the axial direction, the absolute axial velocity (V_x) and the relative axial velocity (W_x) are equivalent (see Equation C2).

$$V_{x1} = W_{x1} \text{ and } V_{x2} = W_{x2} \qquad \textbf{(C2)}$$

An illustration of a linear cascade is shown in Figure C1.

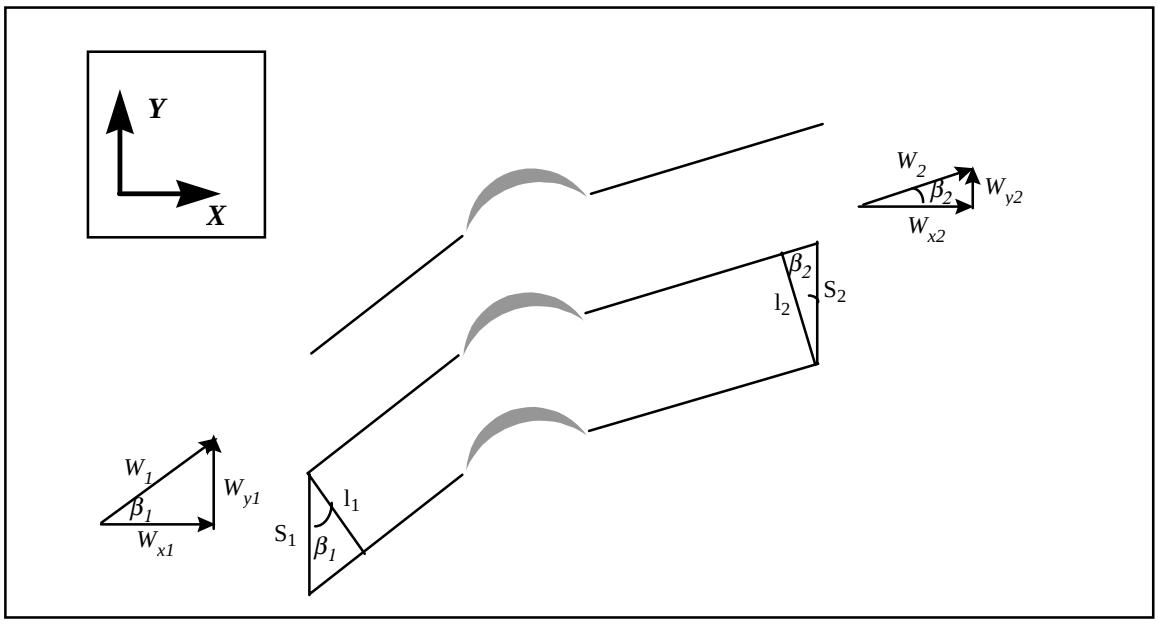

Figure C1 Linear Cascade Flow Properties

Assuming uniform properties, we can solve for A_1/A_2 in terms of the **AVDR** and flow angles β_1 and β_2. Below is a derivation of A_1/A_2 where A_1 and A_2 refer to the cross-sectional areas that are perpendicular to the relative flow at the blade inlet and exit, respectively. Area A_x is the cross-sectional area of the streamtube normal to the axial direction, β is the relative flow angle, d is the uniform depth, $\dot{m}$ is the mass flow rate, and the remaining variables are defined as in Figure C1.

$$A_{x1}/A_{x2} = (S_1*d_1) / (S_2*d_2) \quad \textbf{(C3)}$$

$$A_1/A_2 = (l_1*d_1) / (l_2*d_2) \quad \textbf{(C4)}$$

$$l_1 = S_1* \text{Cos}(\beta_1) \text{ and } l_2 = S_2* \text{Cos}(\beta_2) \quad \textbf{(C5)}$$

$$A_1 = A_{x1} * \text{Cos}(\beta_1) \text{ and } A_2 = A_{x2} * \text{Cos}(\beta_2) \quad \textbf{(C6)}$$

$$A_1/A_2 = A_{x1}/A_{x2}* \text{Cos}(\beta_1) / \text{Cos}(\beta_2) \quad \textbf{(C7)}$$

From conservation of mass we know that

$$\dot{m} = (\rho_1 A_{x1} W_{x1}) = (\rho_2 A_{x2} W_{x2}) \quad \textbf{(C8)}$$

$$A_{x1}/A_{x2} = (\rho_2 W_{x2}) / (\rho_1 W_{x1}) = \textbf{AVDR} \quad \textbf{(C9)}$$

Combining Equations (C7) and (C9) results in

$$A_1/A_2 = \textbf{AVDR}^* \cos(\beta_1) / \cos(\beta_2) \qquad \textbf{(C10)}$$

Note that A_{x1} and A_{x2} do not include the blockage due to boundary layers. Therefore, the **AVDR** cannot be measured strictly from the geometry of the casing although that usually provides a good approximation.

Annular Cascade Theory

Unlike linear cascades in which the relative flow velocity vectors can be described as 2-D, the relative flow in annular cascades is 3-D. Therefore, the areas perpendicular to the relative flow differ from those in Equation (C10). However, if we define a new variable called the Meridional Velocity Density Ratio, **MVDR**, an analogy to the **AVDR** is obtained. The meridional velocity is the vector sum of the axial and radial velocity vectors. The following is the definition of the **MVDR**:

$$\textbf{MVDR} = (\rho_2 V_{m2}) / (\rho_1 V_{m1}) \qquad \textbf{(C11)}$$

where V_m is the absolute meridional velocity. Because the blade velocity is perpendicular to the meridional velocity, the absolute meridional velocity (V_m) and the relative meridional velocity (W_m) are equivalent.

$$V_{m1} = W_{m1} \text{ and } V_{m2} = W_{m2} \qquad \textbf{(C12)}$$

Figure C2 shows the front and side views of an annulus.

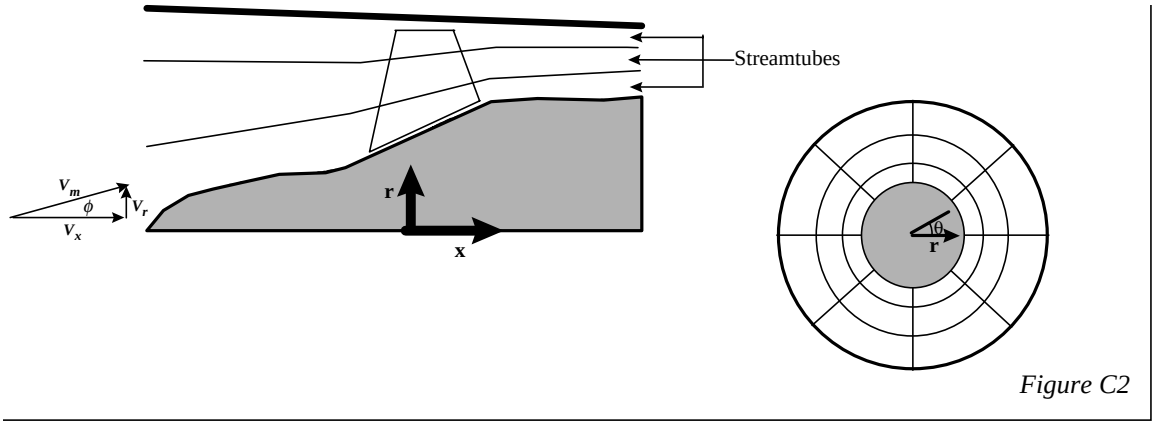

Figure C2 Front and Side Views of a 3-D Annulus

One difference between a 2-D linear and a 3-D annular cascade flow with radial effects is that the 3-D relative flow angles are taken with respect to the meridional velocity as opposed to the axial. Assuming uniform properties and axisymmetric flow where A_m is the cross sectional area of the streamtube normal to the meridional velocity, the derivation of A_1/A_2 is as follows:

Continuity states that

$$\dot{m} = (\rho_1 A_1 W_1) = (\rho_2 A_2 W_2) \quad \textbf{(C13)}$$

$$\therefore A_1/A_2 = (\rho_2 W_2) / (\rho_1 W_1) \quad \textbf{(C14)}$$

Continuity also states that

$$\dot{m} = (\rho_1 A_{m1} W_{m1}) = (\rho_2 A_{m2} W_{m2}) \quad \textbf{(C15)}$$

Combining Equations (C13) and (C15) results in

$$A_1 = A_{m1} * W_{m1}/W_1 \text{ and } A_2 = A_{m2} * W_{m2}/W_2 \quad \textbf{(C16)}$$

The velocity triangles produce

$$\text{Cos}(\beta_1) = W_{m1}/W_1 \text{ and } \text{Cos}(\beta_2) = W_{m2}/W_2 \quad \textbf{(C17)}$$

$$\text{Hence } A_1/A_2 = A_{1m}/A_{2m} * \text{Cos}(\beta_1) / \text{Cos}(\beta_2) \quad \textbf{(C18)}$$

$$\text{So that } A_1/A_2 = \textbf{MVDR} * \text{Cos}(\beta_1) / \text{Cos}(\beta_2) \quad \textbf{(C19)}$$

Hence, there exists a relationship between **AVDR** and **MVDR** that can be derived from velocity triangles:

$$\textbf{MVDR} = \textbf{AVDR} * \text{Cos}(\phi_1)/\text{Cos}(\phi_2) \quad \textbf{(C20)}$$

Chapter 10.0 APPENDIX D Superposition of Loss Terms

This derivation evolved in the exploration of superposing individual loss mechanisms. Because loss is a method for quantifying entropy generation, each loss mechanism correspondingly generates entropy. If these mechanisms behaved linearly, then superposition of entropy would result in the total entropy and therefore the total loss. The author knows of no investigator who currently employs this method of calculating total loss. It is common, however, for simulations to sum individual loss calculations. The derivation below demonstrates the difference between these two methods of calculating total loss. For simplicity, it is shown for a 2-D linear cascade. However, a similar result can be demonstrated for a 3-D annular cascade.

Method 1: Total Loss Calculation using Superposition of Entropy

From the definition of loss,

$$\bar{\omega}_T = (P_{t1} - P_{t2}) / (P_{t1} - P_1)$$

$$\bar{\omega}_T = (1 - P_{t2}/P_{t1}) / (1 - P_1/P_{t1})$$

Assuming a perfect gas with no work or heat transfer along streamline,

$$P_{t2}/ P_{t1} = e^{- \Delta S_T / R}$$

$$\therefore \bar{\omega}_T = (1 - e^{- \Delta S_T / R}) / (1 - P_1/P_{t1})$$

In order to further simplify the analysis, assume that the only two mechanisms that contribute to loss are shocks and boundary layers. Superposing the entropy generated from each mechanism we obtain

$$\Delta S_T = \Delta S_{SH} + \Delta S_{PR}$$

$$\bar{\omega}_T = (1 - e^{- (\Delta S_{SH} + \Delta S_{PR})/ R}) / (1 - P_1/P_{t1})$$

$$\bar{\omega}_T = (1 - e^{- \Delta S_{SH}/ R} * e^{- \Delta S_{PR} / R}) / (1 - P_1/P_{t1}) \qquad \textbf{(10.1)}$$

Method 2: Total Loss Calculations using Superposition of Loss Mechanisms

Summing the loss terms we obtain

$$\bar{\omega}_T = \bar{\omega}_{SH} + \bar{\omega}_{PR}$$

$$\bar{\omega}_{PR} = (1 - e^{- \Delta S_{PR} / R}) / (1 - P_1/P_{t1})$$

$$\bar{\omega}_{SH} = (1 - e^{- \Delta S_{SH} / R}) / (1 - P_1/P_{t1})$$

$$\bar{\omega}_T = [\quad (1 - e^{- \Delta S_{SH} / R}) + \quad (1 - e^{- \Delta S_{PR} / R}) \quad] / \ (1 - P_1/P_{t1})$$

which reduces to

$$\bar{\omega}_T = [2 - (e^{- \Delta S_{SH} / R} + e^{- \Delta S_{PR} / R}) \quad] / \ (1 - P_1/P_{t1}) \qquad \textbf{(10.2)}$$

Clearly, Equations (10.1) and (10.2) are not mathematically equivalent. However, an analysis showed that for the low levels of losses found in Rotor 1-B and Stage 35, there was less than a 0.5% difference in total loss between the two methods. Because it is known that the mechanisms do not behave completely linearly as assumed, either method can be considered a satisfactory estimate.

Chapter 11.0 APPENDIX E A Method for Including Radial Effects

It is clearly evident that radial effects must be accounted for in order to relate losses which occur in 2-D cascades to those in 3-D annular cascades. In an effort to accomplish this relation the following derivations were performed:

3-D Loss Derivation:

$$\bar{\omega}_{3D} = \left(\frac{P_{tr2ideal} - P_{tr2}}{P_{tr1} - P_1} \right) \tag{11.1}$$

$$\bar{\omega}_{3D} = \frac{P_{tr2idea}}{P_{tr1}} \left(\frac{1 - \frac{P_{tr2}}{P_{tr2idea}}}{1 - \frac{P_1}{P_{tr1}}} \right) \tag{11.2}$$

If we assume a perfect gas with no work or heat transfer along a streamline then

$$\frac{P_{tr2}}{P_{tr2idea}} = e^{-\Delta S_{T3D} / R} \tag{11.3}$$

$$\bar{\omega}_{3D} = \frac{P_{tr2idea}}{P_{tr1}} \left(\frac{1 - e^{\frac{-\Delta S_{T3D}}{R}}}{1 - \frac{P_1}{P_{tr1}}} \right) \tag{11.4}$$

2-D Loss Derivation:

$$\bar{\omega}_{2D} = \left(\frac{P_{t1} - P_{t2}}{P_{t1} - P_1} \right) \tag{11.5}$$

$$\bar{\omega}_{2D} = \left(\frac{1 - \frac{P_{t2}}{P_{t1}}}{1 - \frac{P_1}{P_{t1}}} \right) \tag{11.6}$$

If we assume a perfect gas with no work or heat transfer along streamline then

$$\frac{P_{t2}}{P_{t1}} = e^{-\Delta S_{T2D} / R} \tag{11.7}$$

$$\bar{\omega}_{2D} = \left(\frac{1 - e^{\frac{-\Delta S_{T2D}}{R}}}{1 - \frac{P_1}{P_{t1}}} \right) \tag{11.8}$$

Assuming the inlet relative Mach number of the 2-D linear cascade is the same as the relative inlet Mach number of the rotor at the streamline being analyzed, and that $\Delta S_{3D} \cong \Delta S_{2D}$, then

$$\overline{\omega}_{3D} \cong \left(\frac{P_{tr2_{ideal}}}{P_{tr1}} \right) \overline{\omega}_{2D} \qquad \textbf{(11.9)}$$

where

$$\frac{P_{tr2\ ideal}}{P_{tr1}} = \left\{ 1 + \frac{\gamma - 1}{2} * \frac{(\Omega\, r_2)^2}{\gamma\, R\, T_{tr1}} \left[1 - (r_1/r_2)^2 \right] \right\}^{\gamma/(\gamma-1)} \qquad \textbf{(2.4)}$$

VITA

Joseph E. Cahill was born January 10, 1973 in Honolulu, Hawaii. As a member of a military family he spent much of his youth living various places all over the globe. He graduated in 1991 from Lake Braddock High School in Fairfax, Virginia. He matriculated at Virginia Tech the following semester, where he has studied ever since. He completed his B.S. in Mechanical Engineering in May 1995 and began his graduate work the following semester. He spent Summer 1996 working at the Arnold Engineering Development Center in Tullahoma, Tennessee. After completion of this M.S. thesis, he will join a professional golf tour and travel across the country seeking fame and fortune.